Transformation of value signaling in a striatopallidal circuit

Donghyung Lee[1], Lillian Liu[1], and Cory M. Root[1]

[1] University of California San Diego, Department of Neurobiology, School of Biological Sciences, San Diego, California

Abstract

The ways in which sensory stimuli acquire motivational valence through association with other stimuli is one of the simplest forms of learning. Though we have identified many brain nuclei that play various roles in reward processing, a significant gap remains in understanding how value encoding transforms through the layers of sensory processing. To address this gap, we carried out a comparative investigation of the olfactory tubercle (OT), and the ventral pallidum (VP) - 2 connected nuclei of the basal ganglia which have both been implicated in reward processing. First, using anterograde and retrograde tracing, we show that both D1 and D2 neurons of the OT project primarily to the VP and minimally elsewhere. Using 2-photon calcium imaging, we then investigated how the identity of the odor and reward contingency of the odor are differently encoded by neurons in either structure during a classical conditioning paradigm. We find that VP neurons robustly encode value, but not identity, in low-dimensional space. In contrast, OT neurons primarily encode odor identity in high-dimensional space. Though D1 OT neurons showed larger response vectors to rewarded odors than other odors, we propose this is better interpreted as identity encoding with enhanced contrast rather than as value encoding. Finally, using a novel conditioning paradigm that decouples reward contingency and licking vigor, we show that both features are encoded by non-overlapping VP neurons. These results provide a novel framework for the striatopallidal circuit in which a high-dimensional encoding of stimulus identity is collapsed onto a low-dimensional encoding of motivational valence.

Introduction

Animals exhibit an impressive ability to change how sensory inputs map onto behavioral outputs. Understanding how animals learn to output different behaviors through experience is one of the fundamental problems in neuroscience. Over the last half century, the field has developed compelling frameworks to tackle this problem at both the algorithmic level (Rescorla-Wagner models, Q-learning models) (Rescorla, 1972; Sutton, 1988) and the mechanistic level (Hebbian learning, STDP, neuromodulation) (Dan and Poo, 2004). By comparison, we lack frameworks through which to understand how the brain might implement learning algorithms through the updating of synaptic weights. One strategy has been to identify neural correlates of latent features assumed to be required for these algorithms (e.g. dopamine as a neural substrate for reward-prediction-error) (Hollerman and Schultz, 1998; Schultz et al., 1997). These results, however, can often be difficult to interpret because reward related signals are found globally throughout the brain (Allen et al., 2019), and are likely multiplexed with signals about motor output and/or stimulus identity. We propose that a more powerful approach is one that compares 1) how the encoding of reward cues changes from one brain nucleus to its downstream target and 2) how much of the encoding can be explained by value vs. other features such as identity or motor output. In this present work, we implement this comparative approach to the investigation of how encoding of olfactory reward cues is transformed between the olfactory tubercle (OT) and the ventral pallidum (VP) in the context of classical conditioning.

The OT, also known as the tubular striatum (Wesson, 2020), is a 3-layered striatal nucleus situated at the bottom of the forebrain. As with other striatal structures, the OT is composed primarily of Spiny Projection Neurons (SPN's) which express either the *Drd1* or *Drd2* DA receptors (abbreviated as OT_{D1} and OT_{D2}, respectively) (Tritsch and Sabatini, 2012). In addition to receiving a wide range of inputs from cortical and amygdalar areas (e.g. AI, OFC, BLA, PlCoA, Pir) (Zhang et al., 2017b), it receives dense DAergic input from the midbrain (Ikemoto, 2007) and direct input from the mitral and tufted cells of the olfactory bulb (Haberly and Price, 1977; Igarashi et al., 2012; Scott, 1981), a unimodal and primary sensory area. There is a range of experiments that suggest that the OT's DAergic innervation is involved in reward processing. Coincident stimulation of the lateral olfactory tract and DAergic midbrain afferents supports LTP of excitatory current (Wieland et al., 2015) and rats self-administer cocaine, a DAergic drug, into the medial OT more vigorously than to any other striatal nuclei (Ikemoto,

2003). And while the OT neurons are known to respond to a wide range of odorants (Wesson and Wilson, 2010), pairing stimulation of midbrain DAergic neurons with an odor drives appetitive behavior towards the paired odor (Zhang et al., 2017a) and enhances the contrast of the odor-evoked activity (Oettl et al., 2020). Lastly, a number of recent publications report varying degrees of value signals recorded from neurons in the OT (Gadziola et al., 2020, 2015; Martiros et al., 2022; Millman and Murthy, 2020; Oettl et al., 2020).

The most well-established target of the OT is the VP (Newman and Winans, 1980; Zahm and Heimer, 1987), a pallidal structure that lies immediately dorsal to the OT. In addition to OT input, VP receives strong input from the nucleus accumbens (Jones and Mogenson, 1980) and the subthalamic nucleus (Ricardo, 1980; Turner et al., 2001). More recently, it was reported that VP also receives inputs from several cortical and amygdalar areas that also project to the OT (e.g. Pir, BLA, OFC) (Stephenson-Jones et al., 2020). The VP contains GABAergic neurons, which respond to positive value cues, and glutamatergic neurons, which respond to negative value cues. Consistent with their responsiveness, the GABAergic and glutamatergic neurons drive real time place preference and avoidance, respectively (Faget et al., 2018). Though it is well-established that the VP plays a critical role in reward processing, there has been ongoing disagreement on what specific latent features are encoded by VP neurons. Interpretations have included value (Ottenheimer et al., 2018, 2020b; Richard et al., 2016; Tachibana and Hikosaka, 2012), hedonics (Smith et al., 2009; Tindell et al., 2006), motivation (Faget et al., 2018; Fujimoto et al., 2019; Lederman et al., 2021; Tindell et al., 2005), and reward-prediction error (Ottenheimer et al., 2020a). This ongoing discussion highlights the need to adopt a more comparative approach outlined above.

Here, we investigated the transformation of value encoding between the OT and the VP. We began by refining our understanding of OT's efferents to reveal that, contrary to a previous report, both OT_{D1} and OT_{D2} neurons project primarily to the ventrolateral portion of the VP and minimally elsewhere. Given this finding that VP may be the only robust output of the OT, we proposed that the OT to VP circuit is an ideal model system for examining how the encoding of reward cues is transformed between connected brain areas. Comparing the stimulus-evoked activity in OT_{D1}, OT_{D2}, and VP neurons with 2-photon Ca^{2+} imaging, we found that VP neurons encode reward-contingency in low-dimensional space with good generalizability. In contrast, activity in both OT_{D1} and OT_{D2} neurons was high-dimensional and primarily contained information about odor identity. By examining the same neurons across multiple days of pairing,

83 we propose a putative cellular mechanism for reward-cue responsiveness in VP wherein reward
84 responsive VP neurons gradually become reward-cue responsive. Finally, using a novel
85 classical conditioning paradigm, we provide evidence that non-overlapping sets of VP neurons
86 contain information about the vigor of licking and reward-contingency, but not both.

Results

In order to compare odor-evoked activity in connected brain nuclei, we first characterized which specific subregions of the VP receive input from the anteromedial portion of the OT. While considerable effort has been made to unravel the anatomy and function of the NAc, much less attention has been directed at the OT. Though multiple studies have characterized its anatomical connectivity (Zahm and Heimer, 1987; Zhang et al., 2017b; Zhou et al., 2003), there is inconsistency regarding whether or not OT projects to areas other than the VP. We therefore aimed to clarify previously reported OT connectivity by independently conducting anterograde viral tracing experiments in OT_{D1} and OT_{D2} neurons. To this end, we injected AAVDJ-hSyn-FLEX-mRuby-T2A-syn-eGFP in the anterior OT of *Drd1*-Cre (labels D1+ SPN's) and *Adora2a*-Cre (labels D2+ SPN's) animals (Fig1A, FigS1C-E). Because viral contamination of areas dorsal to the target site can lead to difficulties in interpretation of tracing data, we also injected the same virus to the AcbSh immediately dorsal to the OT for comparison. Consistent with past findings (Kupchik et al., 2015), we observed robust projections VP, LH, and VTA from $AcbSh_{D1}$ neurons and primarily VP projections $AcbSh_{D2}$ neurons (Fig1B-C). We also observed dense labeling of the VP in D1-Cre and A2A-Cre animals injected at the OT. Contrary to one report (Zhang et al., 2017b) but consistent with another (Zhou et al., 2003), we observed minimal labeling in LH and VTA, or anywhere else in the brain, for both OT_{D1} and OT_{D2} experiments (Fig1B-C, FigS1A-B), suggesting that neither OT subpopulation projects strongly outside the VP. As previously reported (Groenewegen and Russchen, 1984). It is also notable that OT projections were restricted to the lateral portions of the VP.

To corroborate and more precisely describe the OT to VP projection, we conducted retrograde tracing by injecting CTB::488 and CTB::543 to the lateral and medial portion of caudal VP, respectively (Fig1D, FigS1F-G). We found strong labeling of soma by both CTB::488 and CTB::543 in the Acb, AI, and Pir (Fig1E-F). By comparison, we found predominantly CTB:488, but not CTB::543, labeling in OT soma, indicating OT neurons are more likely to project to the lateral portion of the VP than to the medial. Similarly, to corroborate the lack of OT to VTA projection, we injected CTB::647 into the VTA (Fig1G, FigS1H-I). Consistent with previous findings (Beier et al., 2015; Faget et al., 2016; Watabe-Uchida et al., 2012), we found dense labeling of soma in various areas of the striatum such as AcbSh, AcbC, and CPu (Fig1H-I). We also found some labeling of soma in some frontal cortical regions such as PrL, AI and IL

118 cortices. In stark contrast, we found that hardly any OT neurons were labeled. The rare OT
119 neurons that did have CTB labeling were exclusively localized to the dorsalmost portion of layer
120 III, closely bordering the VP. Taken together, we conclude that both D1 and D2 SPN's of the OT
121 project primarily to the lateral portion of the VP and negligibly to other brain areas, including the
122 VTA.

123 Once we had identified that OT has extremely constrained outputs to the lateral VP, we
124 set out to comparatively characterize the encoding of reward cue in this striatopallidal circuit.
125 Past analysis of value encoding is confounded by not accounting for the difficult-to-avoid
126 overlaps among identity, salience, and reward contingency. To address this, we carefully
127 designed a 6-odor conditioning paradigm where these factors could be decoupled (Fig2A).
128 During each trial, the animal is exposed to 1 of 6 odors for 2 seconds. At the end of odor
129 delivery, the animal either receives: 2 µl of a 10% sucrose solution (S), 50 ms of airpuff at 70 psi
130 (P) or nothing (X). 3 of the odors are ketones (hexanone, heptanone, octanone) and the rest are
131 terpenes (terpinene, pinene, limonene), but the pairing contingencies are chosen such that each
132 contingency group (S, P, or X) includes 1 ketone and 1 terpene. In a value-encoding population,
133 but not in an identity-encoding population, we should see that odor pairs of different reward-
134 contingency (e.g. S_K, a sucrose-paired ketone vs. S_P, an airpuff-paired ketone) are more
135 different than odor pairs of same reward-contingency (e.g. S_K, a sucrose-paired ketone vs. S_T, a
136 sucrose-paired terpene). Additionally, because both sucrose-pairing and airpuff-pairing should
137 make the associated odor more salient, we can disambiguate between increased
138 discriminability due to salience vs. valence by comparing neural activity in response to sucrose-
139 cues or airpuff-cues.

140 To record the activity of the OT and VP neurons across multiple days of pairing, we
141 injected C57BL/6 mice with AAV9-hSyn-jGCaMP7s-WPRE (lateral VP) and *Drd1*-Cre or
142 *Adora2a*-Cre animals with AAV9-hSyn-FLEX-jGCaMP7s-WPRE (anteromedial OT) (Fig2B,
143 FigS2A-F). Additionally, we implanted a 600µm Gradient Refractive Index (GRIN) lens 150µm
144 dorsal to the virus injection site and cemented a head-fixation plate to the skull. 6-8 weeks after
145 surgery, animals were water-restricted and habituated for 3-5 days in the head-fixation setup
146 (Fig2C). We processed the acquired time-series images using Constrained Nonnegative Matrix
147 Factorization (Pnevmatikakis et al., 2016) to obtain fluorescence traces from each putative
148 neuron (Fig2D,E). In total, we recorded Ca^{2+} signals from 231 OT_{D2} neurons from 6 *Adora2a*-

149 Cre animals (FigS3), 288 OT_{D1} neurons from 6 *Drd1*-Cre animals (FigS4) and 130 VP neurons
150 from 5 C57BL6/J animals (FigS5).
151 After 3 days of odor-sucrose associations, the animals displayed anticipatory licking
152 behavior primarily during sucrose-paired odors (Fig2F,G). Starting on day 4, the sucrose and
153 airpuff contingencies were switched such that every odor had a reassigned contingency. By day
154 6, animals had adapted their anticipatory licking behavior to match the new sucrose-contingency
155 (Fig2G). Quantification of the animal's licking behavior showed that the accuracy of animals'
156 licks during odor increased across time and was not different across lens-placement groups
157 (Fig2H; F_{day}=27.64, p_{day}=2.29e-16, $F_{lens\ location}$=2.30, $p_{lens\ location}$=0.11). These results show that the
158 animals learn to associate S odors with reward in a flexible manner in our paradigm. Because
159 we saw the strongest behavioral evidence that animals learned odor-sucrose associations by
160 day 6, we focused our analysis on how reward cues are encoded on the last day of imaging.
161 The animals also showed trends of behavioral changes in response to airpuff-cues, though they
162 were not significant: during airpuff-cues, animals walked less and closed their eyes more than
163 during other odors (FigS6D-G). These behavioral changes for aversive cues were less robust
164 than that for reward association, however, animals show clear responses to the US indicating
165 that they perceive the aversive stimulus.
166 OT and VP neurons showed heterogeneous responses to 6 odors across all 6 days of
167 imaging (FigS3, FigS4, FigS5). To unbiasedly describe the difference between regions, we
168 performed hierarchical clustering on the pooled trial-averaged responses to the 6 odors on the
169 6th day of imaging (Fig3A). We observed both inhibitory (clusters I, II) and excitatory (clusters
170 III-VI) responses to odors as well as broad (clusters II, VI) and narrow (clusters IV, V) odor-
171 tuning (Fig3B). Cluster I and cluster III most closely fit our description of putative valence-
172 encoding neurons, i.e. neurons that had similar responses to 2 sucrose-cues (S_K vs. S_T) but
173 different responses to a sucrose-cue and a puff-cue or control odor (S_K vs. P_K or X_K). Although
174 all clusters included neurons from all subpopulations, cluster I and cluster III, which showed
175 larger responses to odors predicting sucrose, were enriched for VP neurons (Fig3C), leading us
176 to hypothesize that neurons in the VP were more likely to be valence encoding neurons than in
177 either OT subpopulation.
178 To assess this hypothesis, we quantified the number of neurons that had statistically
179 significant responses to each of the 6 odors on the last day of imaging. We found that more VP
180 neurons were either excited (29.8±4.1%, 36.6±4.0% for S_K, S_T) or inhibited (24.5±3.0%,

181 29.4±3.8% for S_K, S_T) to either sucrose-paired odor than to control or puff-paired odors (7.6-
182 11.1% excited, 8.1-12.9% inhibited) (Fig3D,E). A 2-way ANOVA revealed that sucrose-
183 contingency, but not puff-contingency, affects the percentage of responsiveness among VP
184 neurons on day 3 and day 6 (FigS8; F=18.6, p=2.04x10^{-4} and F=32.2, p=5.78x10^{-6},
185 respectively), but not on day 1. By comparison, there was no significant effect of sucrose pairing
186 on the number of responsive neurons among OT_{D2} or OT_{D1} animals on day 6 (p>0.05). OT_{D2}
187 neurons were slightly more responsive to puff-cues on day 3 (FigS8; F=3.03, p=3.99x10^{-2}) and
188 OT_{D1} neurons were more responsive to sucrose-cues on day 3 (FigS8; F=7.33, p=1.08x10^{-2}),
189 but these effects were small when compared to the effect of sucrose pairing observed among
190 VP animals. When compared across days, we found that the percentage of VP neurons that
191 respond to both S odors increases from 6.1±2.2% on day 1 to 34.1±5.1% by the 6th day of
192 imaging (Fig3E). By comparison, the percentage of OT neurons that respond to both S odors in
193 the same direction (i.e. excited by both S odors or inhibited by both S odors) did not increase
194 through training. Furthermore, whereas OT_{D1} and OT_{D2} neurons were more likely to respond to
195 a single odor than they were to respond to both S odors (12.6 vs 31.3% in OT_{D1}, 11.8 vs 21.7%
196 in OT_{D2}), VP neurons were more likely to respond to both S odors than to a single odor (34.1 vs
197 23.3%).
198 Similarly, we found that the magnitude of trial-averaged odor responses in the VP were
199 significantly higher for S odors than X or P odors on the last day of imaging (FigS9; F=59.5,
200 p=3.83x10^{-14}). By comparison, neither sucrose-pairing nor airpuff-pairing had any impact on the
201 magnitude of odor responses in OT_{D2} neurons on day 6. And though we did observe a
202 significant effect of sucrose-pairing on response magnitudes in OT_{D1} neurons (FigS9; F=6.34,
203 p=7.97x10^{-3}), both the effect size and significance were weaker than observed in VP. Given that
204 an ideal value-encoding neuron should respond similarly to 2 odors of equal reward-contingency
205 but disparate molecular structure, we looked at the correlation between each neuron's response
206 to the sucrose-paired ketone (S_K) and to the sucrose-paired terpene (S_T). Consistent with our
207 hypothesis, we saw a high correlation between a VP neuron's responses to S_K and S_T (Fig3F;
208 R^2=0.89). This similarity was much higher than between the sucrose-paired ketone (S_K) and the
209 control ketone (X_K) despite the greater structural similarity between S_K and X_K (Fig3G; R^2=0.33).
210 In contrast, for both OT_{D1} and OT_{D2} neurons, there was a higher correlation between responses
211 to similar molecular structure (S_k and $X_{K,}$) than between responses to similar contingency (S_K
212 and S_T) (OT_{D2}: S_K vs. S_T R^2=0.04, S_K vs. X_K R^2=0.58; OT_{D1}: S_K vs. S_T R^2=0.13, S_K vs. X_K

213 R^2=0.40). Moreover, most VP neurons (76.5%), had a smaller absolute difference in the
214 response magnitude to the 2 S odors ($|S_K-S_T|$) than the absolute difference between the
215 sucrose-paired ketone and the control ketone ($|S_K-X_K|$) (Fig3H). By comparison, only half of
216 OT_{D2} and OT_{D1} neurons showed smaller $|S_K-S_T|$ than $|S_K-X_K|$, as would be expected if response
217 magnitude to an odor did not depend on reward-contingency. This trend was not due to the fact
218 that VP neurons were more likely to respond to both S odors than OT neurons were since it was
219 consistent across various thresholds for odor response magnitude. This trend was consistent for
220 other pairwise odor comparisons where one odor was a sucrose-cue and the other was not (e.g.
221 S_K vs. P_T, FigS10A-B).
222 Finally, we reasoned that the activity of reward-contingency encoding neurons would
223 support good decoding of odor pairs which have different valence but not of odor pairs that have
224 the same valence. To do this, we trained binary logistic classifiers from each neuron's response
225 to all 15 odor pairs and quantified the area under their receiver operating characteristic
226 (auROC). Because auROC values were non-normal with large spread, we quantified what
227 percentage of neurons had an auROC of at least 0.75, halfway between ideal and at-chance
228 decoding. We also note that all classifiers with auROC>0.75 showed bootstrapped p-values less
229 than 10^{-3} (FigS10C-D). To assess whether neurons from each region were encoding valence,
230 we compared a neuron's {S_K vs. X_K} decoder performance (*inter*valence classification) against
231 its {S_K vs. S_T} decoder performance (*intra*valence classification) (Fig3I-J, FigS10E-G). Across
232 multiple days of imaging, we found that the percentage of neurons that support intervalence
233 classification increased regardless of region but that this effect was markedly more pronounced
234 among VP neurons than among OT_{D1} or OT_{D2} neurons (Fig3I, FigS10F). Intravalence
235 classification, however, did not depend on days or region (Fig3J). By day 6, there were thrice as
236 many VP neurons with good intervalence decoding than with intravalence decoding (51.8±5.0%
237 vs. 14.4±5.8% for {S_K vs X_K} and {S_K vs S_T}, respectively). In contrast, a similar number of OT
238 neurons displayed good intervalence decoding as did intravalence decoding (20.8% vs 19.9% of
239 OT_{D1}; 12.8% and 21.0% of OT_{D2} for {S_K vs X_K} and {S_K vs S_T}, respectively). The pattern of
240 better intervalence decoding than intravalence decoding among VP neurons was observed
241 across all 15 pairwise classifiers (FigS10G). Whereas 10.2% of all day 6 VP neurons had
242 auROC>0.75 for {S_K vs. S_T}, 46.9-57.8% had auROC>0.75 for any classification between a
243 sucrose-cue and a control odor or airpuff-cue. By comparison, there were few neurons with

244 auROC>0.75 for any classification between a puff-cue and a control odor (2.3-10.9%),
245 suggesting that negative valence is not encoded in these VP neurons.
246 Plotting a neuron's {S_K vs. S_T} auROC against its {S_K vs. X_K} auROC, we can categorize
247 a neuron into the 4 categories (Fig3K-L). 1) a valence encoding neuron ({S_K vs. S_T}<0.75 and
248 {S_K vs. X_K}>0.75), 2) an identity encoding neuron (both auROC>0.75), 3) an identity encoding
249 neuron that does better with S odors ({S_K vs. S_T}>0.75 and {S_K vs. X_K}<0.75), and 4) an
250 uninformative neuron (both auROC<0.75). According to this categorization, half of VP neurons
251 were valence encoding by day 6, followed by OT_{D1} then OT_{D2} (Fig3M; 47.7, 16.2, 7.3% for VP,
252 OT_{D1}, and OT_{D2}, respectively). The opposite was true for identity encoding. VP had a smaller
253 percentage of identity encoding neurons than either OT_{D1} or OT_{D2} (14.8, 21.1, 22.9% for VP,
254 OT_{D1}, and OT_{D2}, respectively). We note that these conclusions can also be replicated when
255 analyzing multinomial regression (MNR) classifiers trained on single neuron activities (FigS11).
256 Namely, the rates of confusion between the 2 sucrose cues are highest in VP and lowest in
257 OT_{D2} whereas the rates of confusion across all ketones (S_K, X_K, P_K) are highest in OT_{D2} and
258 lowest in VP. These single-neuron classifier analyses further consolidate our hypothesis that VP
259 neurons, more than either OT_{D2} or OT_{D1} neurons, were encoding reward contingency. However,
260 the most striking observation was that while only a subset (37.5%) of VP neurons had
261 auROC<0.75 for both {S_K vs. X_K} and {S_K vs. X_K}, a majority of OT_{D2} and OT_{D1} neurons (69.7%
262 and 62.6%, respectively) showed auROC<0.75 for both {S_K vs. S_T} or {S_K vs. P_K}. This led us to
263 conclude that, in comparison to the VP, most OT neurons have little discriminatory information
264 about olfactory stimuli regardless of valence at the single-neuron level and are rather used in a
265 population code.
266 Our data indicated that valence encoding emerges in VP neurons over the course of
267 learning. To explore the potential mechanisms at the cellular level, we compared the activity of a
268 subset of neurons we could observe on both day 1 and day 3 (Fig4A-F). We noticed there were
269 neurons that responded to the sucrose delivery on day 1 that responded to the sucrose cue on
270 day 3 (Fig4C,F), reminiscent of models of Hebbian plasticity. When quantified, we found that
271 17.9, 20.9% of VP neurons were responsive to sucrose on day 1 and S_K and S_T on day 3,
272 respectively (Fig4G). We specifically considered neurons that had the same direction of
273 response (excitation or inhibition) to both cues on separate days. This figure was much lower
274 among OT subpopulations (11.5, 8.2% for S_K and S_T in OT_{D1}; 10, 2.5% for S_K and S_T in OT_{D2}).
275 Consistent with above observations, we also found that the odor responses to sucrose-cues

were larger on day 3 than day 1 in 85% of tracked VP neurons, but only in 65% and 57% of OT_{D1} and OT_{D2} neurons, respectively (Fig4H,I). We did not see the same effect in VP neurons' responses to control or puff-paired odors. Together, our data suggest that sucrose pairing causes sucrose-responsive VP neurons to increase their responses to the sucrose-predictive odors.

Olfactory brain areas are known to use population codes to encode sensory information. According to this model, single neurons are broadly tuned and their activities have weak discriminatory information. But the activity of the population allows for an efficient encoding of high-dimensional data. To assess if there is discriminatory information about the odorants within the population-level activity, we compared the pairwise euclidean distance of trial-averaged odor responses for all 15 odor pairs (Fig5A,B). We saw that, in general, the pairwise euclidean distance for all odor pairs examined increases quickly after the onset of odor, reaches peak distance towards the end of the 2 second odor delivery, and slowly decays after odor ends (Fig5A). When examining the average pairwise distance during the last second of odor, there was a relatively unstructured distribution of pairwise distance in OT_{D2} odor-response such that $||S_K-X_K||$, $||S_K-P_K||$, $||S_K-S_T||$, and $||X_K-X_T||$ were all similar (Fig5B). By comparison, in VP populations, the distribution was structured such that intervalence pairwise comparisons between sucrose-paired and not sucrose-paired odors (e.g. $||S_K-P_K||$ and $||S_K-X_K||$) were larger than intravalence pairwise comparisons (e.g. $||S_K-S_T||$, or $||X_K-X_T||$). OT_{D1} populations showed an intermediate trend where most intravalence pairwise distances were smaller than intervalence pairwise distances with the exception of $||S_K-S_T||$. Thus, at the population level VP representations appear to encode valence but not identity, whereas OT representations is best suited for identity encoding.

In parallel, we also performed decoding analysis using linear classifiers to assess how reliably a given pair of odors could be decoded from population-level activity (Fig5C-D). To quantify this, we extracted the average $\Delta F_{i,k}/F$ values for each trial $i \epsilon [1,m]$ and each neuron $k \epsilon [1,n]$. The resulting matrix of size m x n was used to train a binary linear classifier with a logistic learner. For each classifier, we looked at the average accuracy across 5-fold cross-validation (CV accuracy). Classifiers were trained on neurons that were recorded together (i.e. neurons from the same animal recorded on the same day) to capture biological variability. A total of 765 pairwise linear classifiers were trained (15 pairwise comparisons, 17 animals and 3 days). When compared against 10,000 shuffles, 569 of these classifiers showed bootstrapped p-value less

308 than 0.001 (FigS12A). Importantly, all classifiers with CV accuracy higher than 0.75 had p-value
309 less than 0.001.
310 Linear classifiers trained on day 6 OT_{D2} population data had similar ranges of accuracy
311 regardless of valence (Fig5D). For example, the intravalence classification {S_K vs. S_T} was more
312 accurate (86.6±3.9**%**) than some and intervalence classifications (e.g. {S_K vs. X_K}, 72.8±5.4**%**)
313 but less accurate than others (e.g. {S_T vs. P_K}, 88.2±3.1**%**). Classifiers trained on VP population
314 activity, however, always showed more accurate intervalence decoding (range: 89.5-96.1%)
315 than intravalence decoding ({S_K vs. S_T}, 79.9±6.1**%)**. Additionally, whereas OT_{D2} population
316 classifiers could decode the 2 control cues {X_K vs. X_T} at accuracy (85.8±4.2**%)** comparable to
317 sucrose-cue vs. non-sucrose-cue, VP population classifiers were consistently less accurate
318 (76.8±3.7**%)** at {X_K vs. X_T} than the aforementioned intervalence classifiers. This suggests that
319 whereas OT_{D2} encodes odor identity agnostic to the valence, VP does not encode identity at all
320 but rather encodes reward contingency or positive value. OT_{D1} pairwise classification was a
321 mixture of the other 2 regions: sucrose-cue vs. non-sucrose-cue classification was more
322 accurate than most other pairwise classifications (range: 86.4-94.3%), but the {S_K vs. S_T}
323 classification was comparably accurate (90.9±4.7%). This rules out the interpretation that OT_{D1}
324 strictly encodes value since the identity of 2 sucrose-cues can be decoded well. To address the
325 possibility that our results are due to the limitations of linear classification, we repeated the
326 analysis using support vector machines (SVM's) with a radial basis function kernel and found
327 we could draw the same conclusions (FigS12E). Similarly, to verify our results are not
328 epiphenomena of forcing the data into binary classification, we looked at population-level MNR
329 classifiers trained on day 6 data. Importantly, we observe high confusion between 2 sucrose
330 cues in MNR classifiers trained on VP data, but not those trained on OT_{D2} or OT_{D1} data
331 (FigS12F), corroborating through an alternate analysis method that VP population activity
332 encodes reward contingency whereas either OT subpopulations likely encode identity.
333 The fact that VP populations showed higher decoding for odor pairs of unequal sucrose-
334 contingency provides strong evidence that VP encodes reward-contingency more than identity.
335 Results from OT decoder analyses, however, are less intelligible: all 15 odor pairs, regardless of
336 sucrose-contingency, could be decoded with above-chance success. Though this result is
337 consistent with OT populations encoding identity rather than valence, it does not rule out the
338 possibility that valence and identity are both encoded. In the context of cue-association, 2 cues
339 of different valence cannot have the same identity, meaning that good decoding of {S_K vs. P_K}

340 can be extracted from either valence encoding or identity encoding populations. To
341 disambiguate these 2 possibilities, we looked at the generalizability of pairwise decoders.
342 Briefly, linear classifiers were trained on each of the 15 possible odor pairs. Afterwards, the
343 resulting classifier was tested on every other odor pair (Fig5E). We reasoned that if neural
344 populations encode valence in addition to identity, classifiers trained on any odor pair of unequal
345 sucrose-contingency should consistently perform above chance on a different odor pair of
346 unequal sucrose-contingency (e.g. train on {S_K vs. P_K}, test on {S_T vs. X_T}). In other words, given
347 valence encoding, {S_K vs. P_K} should be discriminable in a way that can also discriminate {S_T vs.
348 X_T}. As expected, VP population decoders were consistently generalizable when trained on odor
349 pairs of unequal sucrose-contingency then tested on other odor pairs of unequal sucrose-
350 contingency (Fig5F,G). OT_{D2} population decoders, on the other hand, showed negligible
351 generalizability across pairs of unequal sucrose-contingency. Similarly to other metrics of
352 valence encoding, we found that OT_{D1} displayed a generalizability in between that of VP and
353 OT_{D1}, suggesting that OT_{D1} could encode some valence in addition to identity. However, we
354 note that the VP population, on average, vastly outperforms OT_{D1} at generalized valence
355 decoding (95.0±2.0**%** vs 78.5±3.9**%**).
356 After performing these population-level analyses, we noticed a discrepancy: although
357 single-neuron intervalence decoding was worse in OT than in VP (Fig3M), population-level
358 intervalence decoding was comparable between either OT subpopulations and the VP (Fig5A-
359 D). This led us to speculate that the encoding of odor information had a higher dimensionality in
360 OT than in VP. To explicitly compare the dimensionality of VP and OT population activities, we
361 looked at the extent to which the population vector is spread across multiple axes using
362 principal component analysis (PCA). Dimensionality can further be quantified using the
363 participation ratio (PR) of a population, which is the square of the sum of eigenvalues of its
364 covariance matrix divided by the sum of the squares of its eigenvalues (Litwin-Kumar et al.,
365 2017; Recanatesi et al., 2019). This value will have a range of 1 to n, where n is the total
366 number of features. If a single principal component can describe all of the total population
367 variance (i.e. the data is low-dimensional), the population will have PR equal to 1. Conversely, if
368 every principal component equally describes n^{th} of the total variance (i.e. the data is high-
369 dimensional), the population will have PR equal to n. Because the number of total neurons
370 recorded was different between OT and VP experiments, we first assessed if and how the
371 normalized PR would vary with the number of total neurons through random sampling (Fig5H).

372 After observing a consistent decrease in PR with increasing n, we compared the PR of OT and
373 VP animals by repeatedly subsampling a fixed number of neurons (k=15) and found that VP
374 animals had lower PR (PR_{VP} =5.83±0.80) than either OT_{D2} (PR_{D2}=9.61±0.37) or OT_{D1}
375 (PR_{D1}=9.24±0.44) animals after training (Fig5I). There was also a difference, however, in how
376 valence information vs. identity information was encoded by VP populations. Though the first
377 PC of each VP population was sufficient to train adequate {S_K vs. P_K} decoders (CV $accuracy_{PC1}$
378 = 85.5±2.7%), all 15 PC's were required for comparable {S_K vs. S_T} decoding (CV $accuracy_{PC1:15}$
379 = 75.1±13.4%) (Fig5J-L). In either OT populations, the first PC did not support good decoding of
380 either {S_K vs. P_K} or {S_K vs. S_T}. All together, our population-level analysis shows that VP
381 encodes valence, but not identity, in low-dimensional space, OT_{D2} encodes identity but not
382 valence in high-dimensional space, and OT_{D1}, though potentially has valence information,
383 primarily encodes identity in high-dimensional space.
384 Analyses at the single-neuron and population levels showed that VP activity encodes
385 reward contingency, rather than the identity, of the olfactory stimulus. However, due to the task
386 design, the reward-contingency of a stimulus was highly correlated with the vigor of licking
387 (Fig2F). This raised concerns that some neurons classified as robust reward-contingency
388 encoders were potentially encoding motor-related information. Indeed, many VP neurons
389 showed consistent increases in fluorescence time-locked to the onset of a licking-bout
390 (FigS13A-B), and could be used to train distributed lag models to predict onset of licking bouts
391 (FigS13C). Across all VP neurons, we observed a positive and significant correlation between a
392 neuron's valence decoding ability and licking decoding ability (FigS13D; slope=0.41, $p=2.2\times10^{-}$
393 ^{10}, R^2=0.28). This motivated us to develop a new conditioning paradigm that could decouple
394 reward-contingency of an odor cue from the behavioral output.
395 Initially, we attempted to train animals on a symmetric Go/No-Go operant task where
396 reward delivery was contingent on licking or withholding licks during odor. However, consistent
397 with previous findings (Gubner et al., 2010), we found that animals struggled to learn the No-Go
398 behavior in comparison to the Go behavior (data not shown). In an operant paradigm, this leads
399 to a problematic difference in valence of Go/No-Go cues. Consequently, we opted to develop a
400 classical conditioning paradigm whereby licks were encouraged/discouraged by physically
401 moving the lick spout before odor presentation (Fig6A).
402 Briefly, headfixed animals were presented with 1 of 6 odors in pseudorandomized order.
403 During the presentation of 3 of these odors, the lick spout was moved away from the mouse

404 with a linear stepper motor. These odors are denoted as N odors (N for No-lick spout). During
405 the presentation of the other 3 odors, the lick spout remained within licking distance of the
406 mouse's tongue. These odors are referred to as L odors (L for lick spout). 1 odor from each
407 group served as a control odor that had 0% reward-contingency (L_X, N_X). The other 2 odors in
408 each group were paired with sucrose at low (50%) or high (100%) probability (L_{lo}, L_{hi}, N_{lo}, N_{hi}).
409 We reasoned that this contingency could allow us to make pairwise comparisons where one
410 odor has a higher value but lower anticipatory licking than the other (e.g. N_{hi} vs. L_{lo}).
411 To monitor anticipatory licking in the absence of the lick spout, we trained a distributed lag
412 model (DLM) using features of the mouse's face tracked using DeepLabcut (Mathis et al., 2018)
413 (FigS13E-G). We chose to pool data across all mice from the day of the highest licking
414 differential between L_{hi} and N_{hi} odors (FigS13H) to maximize the decoupling of value and motor
415 output in our analysis. Anticipatory licking during L_{lo} or L_{hi} began during the last second of the
416 odor and increased gradually until sucrose delivery whereas licking during N_{lo} or N_{hi} was
417 delayed by about one second (Fig6B). When quantified across animals on their days of highest
418 lick differential, we found that mice consistently licked most during L_{hi}, followed by L_{lo} and N_{hi},
419 then N_{lo} (Fig6C). Mice showed little to no licking during either control odors. Thus, this
420 behavioral assay affords us the opportunity to assess the decoupled effects of reward-
421 contingency and licking vigor on neural activity. To begin to characterize the presence of
422 reward-contingency and/or licking vigor encoding in the VP, we first pooled and clustered the
423 neural activity taken from 5 animals on their days of highest lick-differential (Fig6D). When
424 clustering VP neurons into 3 clusters, we found that one cluster (I) showed a largely similar
425 inhibitory response to the 4 sucrose-paired odors, but not control odors- much like cluster I from
426 the previous conditioning experiment (Fig3A-B, Fig6D-E). Another cluster (II) by comparison,
427 showed a varied excitatory response to each of the 4 sucrose-paired odors, much like cluster III
428 from the previous experiment. Cluster II neurons seemed to have a particularly strong response
429 to L_{hi} for which there was most anticipatory licking. This led us to speculate the existence of both
430 reward-contingency encoding and vigor encoding neurons in the VP.
431 To test this directly, we quantified single neuron decodability of odor pairs and examined
432 how correlated decoding along the reward-contingency axis is to decoding along vigor axis
433 (Fig6F-G). We reasoned that auROC values for {L_{hi} vs. N_{hi}} would be high for vigor encoding
434 neurons but not value encoding neurons given these 2 odors have the same reward-
435 contingency but disparate licking behaviors. Similarly, we reasoned that auROC values for {N_{hi}

436 vs. N_X} would be high for reward-contingency encoding neurons but not vigor encoding neurons
437 given there is a large difference in value but small difference in licking between these 2 odors.
438 First, we saw that while single neuron decodability along the reward-contingency axis (e.g. {N_{hi}
439 vs N_X}) was higher than along the lick axis (e.g. {L_{hi} vs N_{hi}}), there were more neurons that could
440 decode {N_{hi} vs N_X} than could decode {L_X vs N_X} at auROC>0.75 (Fig6F-G). Furthermore, we
441 saw a lack of significant correlation between the single-neuron decodability of 2 odors that had
442 similar licking but different reward-contingency ({N_{hi} vs N_X}) and the decodability of 2 odors that
443 had different licking but same reward-contingency ({L_{hi} vs. N_{hi}}) (Fig6H; slope=0.038, p=0.61,
444 R^2=0.0039). This decoupling suggests that reward-contingency and vigor information are both
445 encoded in the VP but by different populations. As a control, we saw a significant correlation
446 between 2 pairwise comparisons that both had high difference in reward-contingency ({N_{hi} vs
447 N_X} and {L_{hi} vs L_X}) (Fig6I; slope=0.60, p=3.8×10^{-10}, R^2=0.30).
448 We also performed the converse experiment where the $\Delta\Delta F/F_{baseline}$ values of each
449 neuron were linearly fitted to either 1) the reward contingency, 2) the anticipatory licking or 3)
450 both values and the interaction term. Then, we compared the ΔR^2 when either variable was
451 omitted in the model and plotted the $\Delta R^2_{\text{-valence}}$ against the $\Delta R^2_{\text{-licking}}$ (Fig6J). We reasoned that, if
452 a typical VP neuron's activity could be well-explained by either reward-contingency or vigor but
453 not both, we would see points along either x or y-intercepts. On the other hand, if a typical
454 neuron's activity could be well-explained by a linear combination of the 2 variables, we would
455 see data fall along a line of positive slope. We found that most neurons tended to have large
456 $\Delta R^2_{\text{-valence}}$ *or* large $\Delta R^2_{\text{-licking}}$ values but not both, supporting the idea that 2 largely non-
457 overlapping sets of VP neurons encode reward-contingency *or* vigor but not both.
458 Lastly, we trained linear classifiers of pairwise odor comparisons using population-level
459 activity to assess if both reward-contingency and vigor information were present in the
460 population-level activity. Consistent with single-neuron decoder analysis, we found that {L_{hi} vs
461 L_X} and {N_{hi} vs N_X} could both be decoded better than {L_X vs N_X} (Fig6K-L). Because we train
462 each classifier using simultaneously recorded neural activity (i.e. from a single animal), we had
463 a total of 75 classifiers (15 pairwise classifiers for 5 animals). The cross validated accuracies of
464 these classifiers were then fitted to a linear model of pairwise differences in either 1) reward-
465 contingency, 2) anticipatory licking, or 3) both. If the population VP activity encodes either
466 reward-contingency or vigor but not both, we expect to see one of the single-variable models
467 outperform the other greatly. But if the population VP activity encodes both variables, we expect

468 the multivariable model would outperform either single model. We found that Δlicking has a
469 weak and not significant relationship with pairwise CV accuracy (Fig6M; slope=0.076, p=0.079,
470 R^2=0.042). By comparison Δreward-contingency had a larger and statistically significant
471 correlation with pairwise accuracy (Fig6N; slope=0.15, p=3.7×10^{-4}, R^2=0.16). The combined
472 model, however, showed larger coefficients and larger R^2 than either single variable model,
473 suggesting an additive effect of both features on CV accuracy (Fig6O; accuracy = 0.18Δlick +
474 0.24ΔP(S) - 0.22Δlick*ΔP(S) +0.65, R^2=0.23). Thus, we conclude that both reward-contingency
475 and licking vigor are encoded in the population-level activity of VP neurons.

476

Discussion

Our anatomical investigations demonstrate that the primary output of the OT is to the VP, with minimal connections to the VTA. Given its constrained connectivity, we propose that the OT to VP circuit is an ideal model system for examining how the encoding of reward cues is transformed across brain circuits. Utilizing comparative longitudinal imaging, we found that VP, but not OT_{D2}, robustly encodes the sucrose-contingency of odors. Although our analyses revealed that sucrose-contingency influences odor-evoked responses in OT_{D1} neurons more so than in OT_{D2} neurons, other evidence suggests value encoding is not the appropriate framework for interpreting OT_{D1} activity. Specifically, information about sucrose-contingency in OT_{D1} resides in a high-dimensional space and generalizes poorly, whereas VP encodes reward-contingency robustly in a low-dimensional and generalizable manner. Thus, we suggest that the changes in OT_{D1} activity are more likely to reflect increased contrast than value. Finally, using a novel classical conditioning paradigm, we assigned motor-related signals and expected-value signals to non-overlapping VP subpopulations.

Some of our findings were unexpected. For example, we found no evidence that either OT_{D1} or OT_{D2} have significant extrapallidal outputs. This is in direct contrast to a previous study which reported that OT_{D1} neurons, and to a lesser extent, OT_{D2} neurons, project to the LH and VTA (Zhang et al., 2017b). We suspect that at least some of the VTA labeling Zhang and colleagues observed from anterograde viral tracing experiments could be due to backflow of the tracer virus in nuclei immediately dorsal to the OT (e.g. AcbSh). As a critical control, we provide evidence that retrograde tracing from VTA robustly labels AcbSh neurons but hardly any OT neurons. And the few VTA projecting OT neurons we did observe were restricted to the distal portions of layer III bordering the VP. Consistent with this, quantification of OT afferents is glaringly absent from 2 independent characterizations of brainwide inputs onto VTA (Beier et al., 2015; Faget et al., 2016). In contrast, OT has been reported to be one of the most prominent inputs to both GAD2+ and Vglut2+ VP neurons (Stephenson-Jones et al., 2020). We note that another retrograde tracing study (In ’t Zandt et al., 2019) was unable to corroborate reports of OT to OB projections made by Zhang and colleagues from their anterograde viral tracing. This highlights the importance of verifying anterograde tracing experiments with retrograde tracing, especially when the identified output area is also a well-known target of nuclei dorsal to the injection site. It is difficult, however, to completely rule out the existence of OT to midbrain

508 projections due to the limitations of our experiments: we primarily targeted layer II in the
509 anteromedial portion of the OT for anterograde tracing and only tested the VTA with retrograde
510 tracers. More posterior and/or lateral portions of the OT could have extrapallidal outputs
511 posterior to the VTA. Despite these caveats, the evidence strongly suggests that *Drd1*+ neurons
512 in the anteromedial portion of the OT, unlike in the AcbSh, have minimal extrapallidal
513 projections.

514 Interestingly, there is a parallel discrepancy between the anatomical organization of
515 dorsal striatum (DS) vs. ventral striatum (VS): SPN's of the DS project exclusively to either the
516 substantia nigra pars reticulata (SNr) of the midbrain (*Drd1*+) or the exterior portion of the
517 globus pallidus (GPe) (*Drd2*+), but *Drd1*+ neurons in the VS (Acb) project to both the VTA of the
518 midbrain and the ventral pallidum (Kupchik et al., 2015). Our results hint at a gradient of
519 anatomical connectivity where the most dorsal *Drd1*+ SPN's project primarily to the midbrain
520 and the most ventral *Drd1*+ SPN's (i.e. OT_{D1} neurons) project primarily to the pallidum.
521 Functionally, the lack of evidence for OT_{D1} to midbrain connectivity challenges the dichotomy of
522 direct vs. indirect pathways in the ventral basal ganglia. In this model, DA orchestrates motor
523 initiation by oppositely modulating *Drd1*+ and *Drd2*+ SPN's, which have differential downstream
524 targets. Given the lack of clear differences in OT_{D1} and OT_{D2} projections, we think this canonical
525 model of basal ganglia connectivity inadequately explains the functional consequences of DA
526 modulation in the OT.

527 Though we found little difference in the output patterns of OT_{D1} and OT_{D2} neurons, we
528 observed differences in how these 2 subpopulations encode odor valence. Consistent with a
529 previous report (Martiros et al., 2022), we found that OT_{D1} activity, more than OT_{D2} activity, is
530 modulated by reward contingency. For example, OT_{D1} neurons, but not OT_{D2} neurons, were
531 more likely to respond to sucrose-paired odors than other odors. And the magnitude of
532 responses in OT_{D1} but not OT_{D2} neurons were significantly larger to sucrose-paired odors than
533 to other odors. We refrain, however, from concluding that the primary feature encoded in OT_{D1}
534 neurons is value or reward contingency, for the following reasons. First, the above-mentioned
535 effects of sucrose-contingency on neural activity are much stronger for VP than for OT_{D1}.
536 Additionally, whereas more than 50% of VP neurons could be categorized as reward-
537 contingency encoders, this figure was less than 20% for OT_{D1}. Lastly, population-level decoders
538 trained on odor pairs of different valence can generalize in the case of VP populations, but not
539 OT_{D1} populations. While we acknowledge that there is poor standardization when it comes to

defining value encoding, it is unlikely that discrepancies between our conclusions and those of Martiros et al. stem from differences in interpretation alone. Comparative examination of our analyses reveals clear dissimilarities in the effect-size of shared metrics (e.g. % odor responsive). Given the high Z-resolution afforded by 2-photon microscopy, it is probable that we recorded from different layers of the OT, which should not be assumed to have identical physiology. We note that the lens placements in our experiments are considerably more ventral than those reported in Martiros et al. This raises the possibility that some of the neurons recorded in Martiros et al. could be from the rostral portion of the VP which lies immediately dorsal to layer III of the OT. Though *Adora2a* and *Drd1* are not expressed as mRNA in the VP, the BAC-transgenic lines used for both the present work and work by Martiros et al. labels neurons in the VP.

Our comparison of OT and VP is reminiscent of previous comparisons made between value encoding in VP and NAc (Ottenheimer et al., 2018; Richard et al., 2016). These publications showed that VP encodes incentive value more robustly than the NAc. Given that OT and NAc share many anatomical, physiological, and molecular traits, it is tempting to speculate that the encoding schemes, too, would be similar between the 2 areas. Optogenetic activation of OT_{D1} supports RTPP (Murata et al., 2019), as does activation of D1 or D2 neurons of the NAc (Soares-Cunha et al., 2020). While we acknowledge stimulation experiments provide unique insights that cannot be obtained from recordings alone, we note that SPN's have extensive inhibitory collaterals and exhibit high-dimensional activity. Given these peculiarities of the striatum, we predict that bulk stimulation leads to activity patterns so far outside the physiologically relevant range that it warrants conservative extrapolations regarding their endogenous role.

An exciting conclusion from our work is that, within the context of our conditioning paradigm, the dimensionality of neural activity was much lower in VP than in OT. Furthermore, the dimensionality of the imaged subpopulations were anti-correlated with the robustness of sucrose-contingency encoding: OT_{D2} displayed the highest dimensionality and lowest value encoding whereas VP displayed the lowest dimensionality and highest value encoding. As discussed elegantly by others (Chu et al., 2016; Shannon, 1948), there is generally a tradeoff between the efficiency of a neural population (i.e. its total information capacity) and the robustness of its encoding scheme (i.e. redundancy of encoding). Consistently, it is likely that VP neurons display such robust encoding of valence, in large part, due to the loss of odor

identity information. By comparison, OT populations may be able to encode information about the large olfactory identity space due to their high dimensionality. We speculate that the extensive inhibitory collaterals among SPN's play a role in enforcing the high dimensionality of OT activity. Though it is entirely unknown what anatomical or physiological strategies are used to reduce VP dimensionality, we consider this an important piece of the puzzle in understanding VP computations.

We saw little evidence of negative valence neurons in any of the 3 populations that were imaged. This was surprising given previous reports of negative valence neurons in the VP (Stephenson-Jones et al., 2020). We consider 2 potential explanations for this discrepancy. First, it is possible that our conditioning paradigm was not sufficiently aversive for the animals. Although our behavioral evidence for aversive association is significant, it is less robust than sucrose association raising the possibility that the learning was insufficient. This could be due to the fact that we targeted the airpuff to the animal's hindquarters rather than to the face. But we note that in a previous report, airpuff delivery to the snout and to hindquarters elicited similar ingress response in a burrowing assay (Fink et al., 2019). Additionally, we observed clear unconditioned responses to the airpuff itself. For these reasons we think it is more probable that, while negative valence neurons do exist in the VP, as has been reported, they were outside of our field-of-view. Previous work in the VP supports positive and negative valence as being encoded by *Vgat*+ and *Vglut2*+ neurons, respectively (Faget et al., 2018; Stephenson-Jones et al., 2020). Most *Vglut2*+ neurons are found in the dorsomedial portion of the VP, whereas our lenses were specifically targeted to the ventrolateral portion where we found the most OT afferents. Given this distinction, our results are not inconsistent with previous reports of negative valence neurons in the VP.

In our work, we successfully described key differences in how reward cues are encoded in 2 synaptically connected nuclei. But what insights can we infer about the role of OT on shaping VP activity through this comparison? The most salient observation of VP activity is the large and widespread excitatory responses to sucrose-cues. Though the effect size is smaller, OT_{D1} neurons also showed larger excitatory responses to sucrose-cue when compared to other odors. Given that these neurons are GABAergic and their primary target are the VP neurons, it is difficult to explain how these 2 responses are related. We consider 3 possible explanations for this paradox. First, in addition to large excitatory responses that were specific to the sucrose-cues, we also observed inhibitory responses that were specific to the sucrose-cues. It is

604 possible that the excitatory VP activity during sucrose-cue presentation is driven mainly by the
605 numerous excitatory afferents (Pir, BLA, etc.) while the inhibitory VP activity is driven mainly by
606 OT_{D1} and OT_{D2} afferents. In a second model, there could be mechanisms downstream of
607 somatic activity that could explain the discrepancy. For example, though brief optical stimulation
608 of D2 neurons in Acb leads to a decrease of VP activity, prolonged activation causes an
609 increase in VP activity via the δ-opioid receptor (Soares-Cunha et al., 2020). Our experiments
610 do not provide any information on how neuropeptide release from OT neurons is different during
611 presentation of sucrose-cue vs. control odor. Similarly, we cannot measure if and how positively
612 valent stimuli change the input-output-function of OT neurons. Previous reports have found that
613 Drd2 agonism in Acb neurons leads to a decrease in collateral inhibition through a presynaptic
614 mechanism (Dobbs et al., 2016). Given that more DA is expected to be released during
615 presentation of sucrose-cues, it is plausible that the probability of GABA release from OT
616 boutons onto VP dendrites is affected. In a third and perhaps the most parsimonious model,
617 endogenous OT activity does not contribute significantly to explaining the bulk excitatory activity
618 in VP. This goes against the prevailing working model in Acb to VP circuit which assumes that
619 Acb excitation leads to VTA disinhibition by inhibiting the VP. And while there is evidence
620 supporting from bulk stimulation of D1 or D2 neurons in the Acb (Soares-Cunha et al., 2020),
621 under endogenous conditions, both Acb neurons and VP neurons are excited in response to
622 reward-cues (Lederman et al., 2021; Ottenheimer et al., 2018). Furthermore, given that
623 GABAergic synapses from SPN's to VP neurons is likely dendritic (Bolam et al., 1986), we think
624 it is unlikely that OT to VP drives large-scale shunting of action potential in the presence of
625 excitatory drive from other areas known to respond preferentially to reward cues such as the
626 BLA (Beyeler et al., 2018) or the OFC (Wang et al., 2020). We consequently propose an
627 alternate framework in which the mechanistic role of the OT in this circuit is to provide
628 spatiotemporally precise inhibition to coordinate the integration of excitatory inputs onto VP.
629 This form of inhibition could powerfully gate which excitatory synapses go through Hebbian
630 potentiation vs. anti-Hebbian depression. Under such a framework, OT would function as a
631 high-dimensional filter for VP neurons to adaptively scale its various excitatory afferents.
632 In this work, we present evidence that contradict previous anatomical and physiological
633 characterizations of the OT. We conclude that the anteromedial portion of the OT sends high-
634 dimensional information about odor identity primarily to the VP and not the VTA. By directly
635 comparing OT and VP population-level activity in the same paradigm, we bridge together, for

636 the first time, the fields of OT and VP. This provides valuable context which not only helps us
637 evaluate past conclusions about valence encoding in the OT but also consider the implications
638 of the stimulus-evoked activity in the OT. Lastly, we propose a novel framework for
639 understanding the contributions of striatopallidal projections in reward processing. In our
640 framework, OT neurons guide VP's integration of its excitatory afferents rather than being the
641 primary drivers of VP activity. We believe this framework effectively addresses the observed
642 paradox that both OT_{D1} and VP show increased excitatory activity to reward cues despite being
643 connected through inhibitory projections. Furthermore, we speculate this framework will be
644 useful for understanding striatopallidal projections at large.
645
646
647

648 Methods

649 Stereotaxic Surgery:

650 All procedures were approved by the UCSD Institutional Animal Care and Use
651 Committee. Animals were anesthetized with isoflurane (3% for induction, 1.5-2.0% afterward)
652 and placed in a stereotaxic frame (Kopf Model 1900). Mouse blood oxygenation, heart rate and
653 breathing were monitored throughout surgery, and body temperature was regulated using a
654 heating pad (Physio Suite, Kent Scientific). A small craniotomy above the injection site was
655 made using standard aseptic technique. Virus was injected with needles pulled from capillary
656 glass (3-000-203-G/X, Drummond Scientific) at a flow rate of 2nl/s using a micropump (Nanoject
657 III, Drummond Scientific). For OT anterograde tracing experiments, 50µl of AAV9-phSyn1-
658 FLEX-tdTomato-T2A-SypEGFP-WPRE diluted to 10^{12} vg/ml was injected into the rostral portion
659 of the medial OT (AP: 1.6mm, ML: -1.0mm, DV: -5.375mm) in *Drd1*-Cre or *Adora2a*-Cre mice.
660 For VP retrograde tracing experiments, 100 nl of Cholera Toxin Subunit B CF 488A (Biotium)
661 was injected at into the caudal portion of the ventrolateral VP (AP: 0.75mm, ML: -1.4mm, DV: -
662 5.4mm) and 100 nl of Cholera Toxin Subunit B CF 543 (Biotium) was injected into the
663 dorsomedial VP (AP: 0.75mm, ML: -1.0mm, DV: -5.35mm) in C57BL6/J mice. For VTA
664 retrograde tracing experiments, 100 nl of Cholera Toxin Subunit B CF 647 (Biotium) was

665 injected to the rostral portion of the VTA (AP: -3.1mm, ML: 0.8mm, DV: -4.5mm) in C57BL6/J
666 mice. CTB injections were done at 1 mg/ml dilution in PBS. In some cases, tracers were
667 injected bilaterally and each hemisphere was analyzed independently. Following each injection,
668 the injection needle was left at the injection site for 10 minutes then slowly withdrawn.
669 For imaging experiments, the skull was prepared with OptiBond™ XTR primer and
670 adhesive (KaVo Kerr) prior to the craniotomy. After performing a craniotomy 800 um in diameter
671 centered around the virus injection site, a 27G blunt needle was used to aspirate 1.5 mm below
672 the brain surface. For OT imaging experiments, 500 ul of AAV9-syn-FLEX-jGCaMP7s-WPRE
673 (Addgene viral prep #104491-AAV9) was diluted to 10^{12} vg/ml and injected into the left and
674 rostral portion of the medial OT in D1-Cre or A2A-Cre mice. For VP imaging experiments, 300 ul
675 of AAV9-syn-jGCaMP7s-WPRE (Addgene viral prep #104487-AAV9) was diluted to 10^{12} vg/ml
676 and injected into the left and caudal portion of the ventrolateral VP in C57BL6/J mice. Following
677 the viral injection, a head-plate (Model 4, Neurotar) was secured to the mouse's skull using
678 light-curing glue (Tetric Evoflow, Ivoclar Group). At least 30 minutes after viral injection, a
679 600um GRIN lens (NA, ~1.9 pitch, GrinTech) was sterilized with Peridox-RTU then slowly
680 lowered at a rate of 500 um/min into the craniotomy until it was 200 um dorsal to the injection
681 coordinate. The lens was adhered to the surface of the skull using Tetric Evoflow. We then
682 placed a hollow threaded post (AE825ES, Thorlabs) to act as a housing for the lens and
683 adhered it using Tetric Evoflow. Any part of the skull that was still visible was covered using
684 dental cement (Lang Dental). Finally, the housing was covered with a Nylon cap nut
685 (94922A325, McMaster-Carr) screwed onto the thread post to protect the lens in between
686 imaging. Animals were left on the heating pad until they fully recovered from anesthesia.

687 Histology:

688 Mice were administered ketamine (100 mg/kg) and xylazine (10 mg/kg) and euthanized
689 by transcardial perfusion with 10 ml of cold PBS followed by 10 ml of cold 4% paraformaldehyde
690 in PBS. Brains were extracted and left in a 4% PFA solution in PBS overnight. 50 um coronal
691 sections were cut on a vibratome (VT1000, Leica). A subset of tissue was labeled with the
692 following antibodies: Rb α-substance P (1:1,000 dilution; 20064, Immunostar), Rb α-TH (1:1,000
693 dilution; AB152, Millipore), Dk α-Rb Alexa Fluor™ 488 (1:2,000 dilution; A-210206, Thermo
694 Fisher Scientific), Dk α-Rb Alexa Fluor™ 647 (1:2,000 dilution; A-31573, Thermo Fisher
695 Scientific). Slices were mounted using Fluoromount with a DAPI counterstain (SouthernBiotech)

696 and imaged on an Olympus BX61 VS120 Virtual Slide Scanner and 10x objective (Olympus).
697 Brains were harvested 21-30 days or 5-7 days after surgery for anterograde and retrograde
698 tracing experiments, respectively. Brains injected for Ca^{2+} imaging were harvested within a week
699 of the last imaging session.
700 For anterograde tracing quantification, 4-6 slices containing each of the brain regions of
701 interest (VP, LH, and VTA) were analyzed per animal. To quantify the relative abundance of OT
702 axons in a given brain region, boundaries for the region were drawn on ImageJ Fiji (National
703 Institutes of Health) with reference to the Paxinos and Franklin Mouse Brain Atlas. Afterwards,
704 the percentage of the 16-bit pixels within the boundary that had intensity above 200 was
705 quantified. For retrograde tracing experiments, cells were counted manually every 4th slice.
706
707 For anterograde tracing quantification, 4-6 slices containing each of the brain regions of
708 interest (VP, LH, and VTA) were analyzed per animal. To quantify the relative abundance of OT
709 axons in a given brain region, boundaries for the region were drawn on ImageJ Fiji (National
710 Institutes of Health) with reference to the Paxinos and Franklin Mouse Brain Atlas. Afterwards,
711 the percentage of the 16-bit pixels within the boundary that had intensity above 200 was
712 quantified. For retrograde tracing experiments, cells were counted manually every 4th slice.

713 Behavior

714 Mice were water restricted to reach 85-90% of their initial body weight and given access
715 to water for 5 minutes a day in order to maintain desired weight. Prior to imaging, mice were
716 habituated to the head fixation device (Neurotar) and treadmill for 3-5 days, 15-30 minutes per
717 session. The treadmill parts were 3D printed using a LCD printer (X1-N, EPAX) from publicly
718 available designs (Jackson et al., 2018). During habituation, mice were provided 10% sucrose
719 from the water spout. Walking and licking behaviors were measured using a quadrature encoder
720 (HEDR-5420-es214, Broadcom) and a capacitance sensor (1129_1, Phidgets), respectively. A
721 video feed of the animal's face was also recorded using a camera (acA1300-30um, Basler) with
722 a 8-50mm zoom lens (C2308ZM50, Arducam) at 20 Hz with infrared illumination (VQ2121,
723 Lorex Technology).
724 Odor was delivered to the mouse using a custom-built olfactometer. Compressed
725 medical air was split into 2 gas-mass flow controllers (GFC17, Aalborg). One flow controller
726 directed a constant rate of 1.5 L/min to a hollowed out teflon cylinder. The other flow regulator

727 was connected to a 3-way solenoid valve (**LHDB1223418H,** The Lee Co.). Prior to odor delivery,
728 the 3-way valve directs clean air at 0.5 L/min to the teflon cylinder. During odor delivery, the 3-
729 way valve directs air to an odor manifold, which consists of an array of 2-way solenoid valves
730 (LHDB1242115H, The Lee Co.), each connected to a different odor bottle. Depending on the
731 trial type, the appropriate 2-way valve opens, directing 0.5 L/min of air flow through the odor
732 bottle containing a kimwipe blotted with 50 ul of diluted odor. All odors were diluted in mineral oil
733 (M5310, Sigma-Aldrich) to 1.5 mmHg. The kinetics and consistency of odor delivery were
734 characterized for 30 trials of terpinene delivery using a miniature Photoionization Detector
735 (mPID) (Aurora Scientific, Inc).

736 During classical conditioning, animals were exposed to the following odors for 2
737 seconds: 3-hexanone, 3-heptanone, 3-octanone, α-terpinene, α-pinene, and (R)-(+)-limonene
738 (all odors were purchased from Sigma with the highest available purity). In days 1-3 of training,
739 each of the 6 odors and associated outcomes were provided 30 times with 12-18 seconds of
740 inter-trial interval. Hexanone and terpinene were not associated with any outcome, heptanone
741 and pinene were associated with 2 ul of 10% sucrose, and octanone and limonene were
742 associated with a 75 psi airpuff delivered to their hindquarters. Sucrose or airpuff was delivered
743 100-300 ms after the end of odor delivery. Trials were organized into 30 blocks, each of which
744 consisted of 1 trial of each of the 6 odors in randomized order. In days 4-6 of training, the
745 outcome contingencies were switched such that heptanone and limonene were not associated
746 with any outcome, octanone and terpinene were associated with 2 ul of 10% sucrose, and
747 hexanone and pinene were associated with 75 psi airpuff.

748 In the lick-no-lick paradigm, trials were also structured into 30 blocks, each of which
749 consisted of 1 trial of each of the 6 odors in randomized order. Hexanone and terpinene were
750 not associated with any outcome, heptanone and pinene were paired with 2 ul of 10% sucrose
751 at 50% chance, and octanone and limonene were paired with 2 ul of 10% sucrose at 100%
752 chance. 200 ms prior to the onset of 3 of the odors (terpinene, octanone, and limonene), the lick
753 spout was retracted 30 mm away from the animal's mouth using a linear stepper motor (BE073-
754 1, Befenybay) and driver (A4988, BIQU). The lick spout would return to its original position 100
755 ms prior to the earliest possible time of sucrose delivery.

DeepLabCut

DeepLabCut2.3.3 with Tensorflow 2.12 was used to track 4 points on the periphery of the eye during 2-photon Ca^{2+} imaging. The mini-batch k-means clustering method was used to extract a total of 100 frames (20 frames from 5 animals). These frames were labeled and used to train a Deep Neural Network (DNN) model for 100,000 iterations. After the first training session, 20 outlier frames were picked up from each video and added to the training data for a second training session. The area of the eye at a given time point was estimated as an ellipse. For the lick-no-lick paradigm, we used DeepLabCut to track the tip of the tongue, the corner of the mouth, the upper lip and the lower lip. To record licking in the absence of the lick spout, we trained a linear classifier using logistic regression of the following metrics: 1) the confidence score for the tip of the tongue, 2) the confidence score for the corner of the mouth and 3) the Euclidean distance between the upper and lower lip. Data collected from the capacitive lick sensor was used as ground truth for the classifier.

2-photon Ca^{2+} imaging in head-fixed, behaving mice

Mice were habituated to the head-fixation setup for 3 days beginning 8-10 weeks after surgery. Ca^{2+} imaging data was acquired using an Olympus FV-MPE-RS Multiphoton microscope with Spectra Physics MaiTai HPDS laser, tuned to 920 nm with 100 fs pulse width at 80 MHz. Each 128x128 pixel scan was acquired with a 20x air objective (LCPLN20XIR, Olympus), using a Galvo-Galvo scanner at 5Hz. Stimulus delivery and behavioral measurements were controlled through a custom software written in LabVIEW (National Instruments) and operated through a DAQ (USB-6008, National Instruments). Each imaging session lasted between 30-45 minutes and was synchronized with the stimulus delivery software through a TTL pulse. The imaging depth was manually adjusted to closely match that of the first imaging day such that we recorded from overlapping populations across days of imaging. Animals were excluded from analysis if a) histology showed that either the GRIN lens or the jGCaMP7s virus was mistargeted or b) the motion during imaging was too severe for successful motion-correction. 2 animals were excluded due to mistargeting and 2 animals were excluded due to excessive motion.

Image Processing:

Ca^{2+} imaging data were first motion-corrected using the non-rigid motion correction algorithm NoRMCorre (Pnevmatikakis and Giovannucci, 2017). Afterwards, neural traces were extracted from the motion-corrected data using constrained nonnegative matrix factorization (CNMF) (Giovannucci et al., 2019; Pnevmatikakis et al., 2016). Spatial components identified by CNMF were inspected by eye to ensure they were not artifacts. A Gaussian Mixture Model (GMM) was used to estimate the baseline fluorescence of each neuron. To account for potential low-frequency drift in the baseline, the GMM was applied along a moving window of 2,500 frames (500 seconds). The fluorescence of each neuron at each time point *t* was then normalized to the moving baseline to calculate $\Delta F/F = F_t - F_{baseline}/F_{baseline}$. All subsequent analysis was performed using custom code written in MATLAB (R2022b).

Hierarchical clustering of pooled averaged responses

ΔF/F in response to all 6 odors on day 6 were averaged across trials then Z-scored. The resulting trial-average values from the following timebins were averaged across time: 1) the first second during each odor, 2) the last second during each odor, and 3) the first second after each odor. The resulting 18-element vectors were sorted into 6 clusters after agglomerative hierarchical clustering using euclidean distance and ward linkage.

Responsiveness criteria

To determine how many neurons were responsive to a given odor, we compared ΔF/F at each frame during the 2 second odor period against a pooled distribution of ΔF/F values from the 2-seconds prior to odor onset using a Wilcoxon rank sum test. The resulting p-values were evaluated with Holm-Bonferroni correction to ensure that familywise error rate (FWER) was below 0.05. We then calculated the percentage of responsive neurons for each animal to show the mean and the standard error as a function of time. We also counted the number of neurons that were significantly responsive for at least 4 frames during the odor period to report the total percentage of responsive neurons during odor.

Single neuron logistic classifiers

To test how reliably a single neuron's fluorescence could discriminate between 2 odors, we assessed the performance of binary logistic classifiers trained on a single neuron's responses to 2 odors. For each neuron and odor pair, we averaged the ΔF/F during the last second of the odor exposure for each trial then Z-scored across all trials. The resulting 60-element vector was used to train a linear classifier using logistic regression. The receiver operator characteristic (ROC) was evaluated for each single neuron pairwise classifier and the area under the curve (AUC) reported. To test if a given pairwise classifier performed significantly better than chance, we compared the accuracy of each classifier against a distribution of 10,000 classifiers trained on shuffled labels.

Normalized ΔΔF/F correlations

To compare the average response of a neuron to each odor, the trial-averaged ΔF/F during the last second of odor exposure from each trial was averaged and then subtracted from the trial-averaged ΔF/F during the 2 seconds prior to odor delivery. This ΔΔF/F value was scaled to the largest positive ΔΔF/F value of each neuron for all odors. To assess the similarity of the average response to a given pair of odors i and j, we looked at the null linear model in which all neurons respond identically to both odors, i.e. $\Delta\Delta F_j/F = \Delta\Delta F_i/F$. To assess how well this describes the data, we report the R^2 value of the fit.

Pairwise euclidean distance

To quantify the differences among population-level responses to the 6 odors, we quantified the pairwise Euclidean distance between the trajectories of odor responses. First, we subtracted the ΔF/F values during the 2 seconds prior to odor delivery from each frame then averaged these values across trials for each odor. The pairwise Euclidean distance at each frame was computed for each odor pair and normalized to the maximum pairwise distance measured in all odor pairs at any time bin. These calculations were carried out separately for each animal and then averaged across biological replicates to report the mean and the standard error.

Population pairwise classifiers

To assess the discriminability of odor responses in high-dimensional space, we measured the accuracy of binary classifiers for a given odor pair. At each time point relative to odor delivery, we pooled ΔF/F values from all trials during which either odor was presented. These values were then normalized and used to train a linear classifier using either a logistic regression or a Support Vector Machine (SVM). The accuracy of the classifier was evaluated via 5-fold cross-validation. To test if a given pairwise decoder performed significantly better than chance, we compared the accuracy of each classifier against a distribution of 10,000 classifiers trained on shuffled labels. All classifiers were trained on populations of neurons simultaneously recorded from individual mice. The resulting cross-validated accuracies were averaged across biological replicates to report the mean and the standard error.

Dimensionality analysis

To quantify the dimensionality of each simultaneously recorded neural population, we calculated its participation ratio (PR). First, we performed principal component analysis of the whole dataset using the singular value decomposition algorithm. The PR was calculated as the square of the sum of the eigenvalues of the covariance matrix divided by the sum of the square of its eigenvalues (Litwin-Kumar et al., 2017; Recanatesi et al., 2019). To account for the differences in number of recorded neurons across individuals, we bootstrapped the PR by randomly sampling *n* neurons from each dataset 1,000 times and reported the average PR value.

Author contributions

D.L. and C.M.R. conceived of the project, participated in its development and wrote the manuscript. L.L. assisted with anatomy, histology and behavioral analysis. D.L. performed all imaging experiments and analyzed the data.

Acknowledgments

We thank members of Root lab for discussions, M. Aoi for discussions on data analysis, and T. Komiyama and for comments on the manuscript. This research was supported by grants from the NIH (R00DC014516, R01DC018313), and C.M.R. was a Hellman Fellow.

References

Allen WE, Chen MZ, Pichamoorthy N, Tien RH, Pachitariu M, Luo L, Deisseroth K. 2019. Thirst regulates motivated behavior through modulation of brainwide neural population dynamics. *Science* **364**:253.

Beier KT, Steinberg EE, DeLoach KE, Xie S, Miyamichi K, Schwarz L, Gao XJ, Kremer EJ, Malenka RC, Luo L. 2015. Circuit Architecture of VTA Dopamine Neurons Revealed by Systematic Input-Output Mapping. *Cell* **162**:622–634.

Beyeler A, Chang C-J, Silvestre M, Lévêque C, Namburi P, Wildes CP, Tye KM. 2018. Organization of Valence-Encoding and Projection-Defined Neurons in the Basolateral Amygdala. *Cell Rep* **22**:905–918.

Bolam JP, Ingham CA, Izzo PN, Levey AI, Rye DB, Smith AD, Wainer BH. 1986. Substance P-containing terminals in synaptic contact with cholinergic neurons in the neostriatum and basal forebrain: a double immunocytochemical study in the rat. *Brain Res* **397**:279–289.

Chu MW, Li WL, Komiyama T. 2016. Balancing the Robustness and Efficiency of Odor Representations during Learning. *Neuron* **92**:174–186.

Dan Y, Poo M-M. 2004. Spike timing-dependent plasticity of neural circuits. *Neuron* **44**:23–30.

Dobbs LK, Kaplan AR, Lemos JC, Matsui A, Rubinstein M, Alvarez VA. 2016. Dopamine Regulation of Lateral Inhibition between Striatal Neurons Gates the Stimulant Actions of Cocaine. *Neuron* **90**:1100–1113.

Faget L, Osakada F, Duan J, Ressler R, Johnson AB, Proudfoot JA, Yoo JH, Callaway EM, Hnasko TS. 2016. Afferent Inputs to Neurotransmitter-Defined Cell Types in the Ventral Tegmental Area. *Cell Rep* **15**:2796–2808.

Faget L, Zell V, Souter E, McPherson A, Ressler R, Gutierrez-Reed N, Yoo JH, Dulcis D, Hnasko TS. 2018. Opponent control of behavioral reinforcement by inhibitory and excitatory projections from the ventral pallidum. *Nat Commun* **9**:849.

Fink AJP, Axel R, Schoonover CE. 2019. A virtual burrow assay for head–fixed mice measures habituation, discrimination, exploration and avoidance without training. *Elife* **8**:e45658.

Fujimoto A, Hori Y, Nagai Y, Kikuchi E, Oyama K, Suhara T, Minamimoto T. 2019. Signaling Incentive and Drive in the Primate Ventral Pallidum for Motivational Control of Goal-Directed Action. *J Neurosci* **39**:1793–1804.

Gadziola MA, Stetzik LA, Wright KN, Milton AJ, Arakawa K, Del Mar Cortijo M, Wesson DW. 2020. A Neural System that Represents the Association of Odors with Rewarded Outcomes and Promotes Behavioral Engagement. *Cell Rep* **32**:107919.

Gadziola MA, Tylicki KA, Christian DL, Wesson DW. 2015. The olfactory tubercle encodes odor valence in behaving mice. *J Neurosci* **35**:4515–4527.

Giovannucci A, Friedrich J, Gunn P, Kalfon J, Brown BL, Koay SA, Taxidis J, Najafi F, Gauthier JL, Zhou P, Khakh BS, Tank DW, Chklovskii DB, Pnevmatikakis EA. 2019. CaImAn an open source tool for scalable calcium imaging data analysis. *Elife* **8**. doi:10.7554/eLife.38173

Groenewegen HJ, Russchen FT. 1984. Organization of the efferent projections of the nucleus accumbens to pallidal, hypothalamic, and mesencephalic structures: a tracing and immunohistochemical study in the cat. *J Comp Neurol* **223**:347–367.

Gubner NR, Wilhelm CJ, Phillips TJ, Mitchell SH. 2010. Strain differences in behavioral inhibition in a Go/No-go task demonstrated using 15 inbred mouse strains. *Alcohol Clin Exp Res* **34**:1353–1362.

Haberly LB, Price JL. 1977. The axonal projection patterns of the mitral and tufted cells of the

olfactory bulb in the rat. *Brain Res* **129**:152–157.
Hollerman JR, Schultz W. 1998. Dopamine neurons report an error in the temporal prediction of reward during learning. *Nat Neurosci* **1**:304–309.
Igarashi KM, Ieki N, An M, Yamaguchi Y, Nagayama S, Kobayakawa K, Kobayakawa R, Tanifuji M, Sakano H, Chen WR, Mori K. 2012. Parallel mitral and tufted cell pathways route distinct odor information to different targets in the olfactory cortex. *J Neurosci* **32**:7970–7985.
Ikemoto S. 2007. Dopamine reward circuitry: two projection systems from the ventral midbrain to the nucleus accumbens-olfactory tubercle complex. *Brain Res Rev* **56**:27–78.
Ikemoto S. 2003. Involvement of the olfactory tubercle in cocaine reward: intracranial self-administration studies. *J Neurosci* **23**:9305–9311.
In ’t Zandt EE, Cansler HL, Denson HB, Wesson DW. 2019. Centrifugal Innervation of the Olfactory Bulb: A Reappraisal. *eNeuro* **6**. doi:10.1523/ENEURO.0390-18.2019
Jackson J, Karnani MM, Zemelman BV, Burdakov D, Lee AK. 2018. Inhibitory Control of Prefrontal Cortex by the Claustrum. *Neuron* **99**:1029–1039.e4.
Jones DL, Mogenson GJ. 1980. Nucleus accumbens to globus pallidus GABA projection: electrophysiological and iontophoretic investigations. *Brain Res* **188**:93–105.
Kupchik YM, Brown RM, Heinsbroek JA, Lobo MK, Schwartz DJ, Kalivas PW. 2015. Coding the direct/indirect pathways by D1 and D2 receptors is not valid for accumbens projections. *Nat Neurosci* **18**:1230–1232.
Lederman J, Lardeux S, Nicola SM. 2021. Vigor Encoding in the Ventral Pallidum. *eNeuro* **8**. doi:10.1523/ENEURO.0064-21.2021
Litwin-Kumar A, Harris KD, Axel R, Sompolinsky H, Abbott LF. 2017. Optimal Degrees of Synaptic Connectivity. *Neuron* **93**:1153–1164.e7.
Martiros N, Kapoor V, Kim SE, Murthy VN. 2022. Distinct representation of cue-outcome association by D1 and D2 neurons in the ventral striatum’s olfactory tubercle. *Elife* **11**. doi:10.7554/eLife.75463
Mathis A, Mamidanna P, Cury KM, Abe T, Murthy VN, Mathis MW, Bethge M. 2018. DeepLabCut: markerless pose estimation of user-defined body parts with deep learning. *Nat Neurosci* **21**:1281–1289.
Millman DJ, Murthy VN. 2020. Rapid Learning of Odor–Value Association in the Olfactory Striatum. *J Neurosci* **40**:4335–4347.
Murata K, Kinoshita T, Fukazawa Y, Kobayashi K, Yamanaka A, Hikida T, Manabe H, Yamaguchi M. 2019. Opposing Roles of Dopamine Receptor D1- and D2-Expressing Neurons in the Anteromedial Olfactory Tubercle in Acquisition of Place Preference in Mice. *Front Behav Neurosci* **13**:50.
Newman R, Winans SS. 1980. An experimental study of the ventral striatum of the golden hamster. II. Neuronal connections of the olfactory tubercle. *J Comp Neurol* **191**:193–212.
Oettl L-L, Scheller M, Filosa C, Wieland S, Haag F, Loeb C, Durstewitz D, Shusterman R, Russo E, Kelsch W. 2020. Phasic dopamine reinforces distinct striatal stimulus encoding in the olfactory tubercle driving dopaminergic reward prediction. *Nat Commun* **11**:3460.
Ottenheimer DJ, Bari BA, Sutlief E, Fraser KM, Kim TH, Richard JM, Cohen JY, Janak PH. 2020a. A quantitative reward prediction error signal in the ventral pallidum. *Nat Neurosci* **23**:1267–1276.
Ottenheimer DJ, Wang K, Tong X, Fraser KM, Richard JM, Janak PH. 2020b. Reward activity in ventral pallidum tracks satiety-sensitive preference and drives choice behavior. *Sci Adv* **6**. doi:10.1126/sciadv.abc9321
Ottenheimer D, Richard JM, Janak PH. 2018. Ventral pallidum encodes relative reward value earlier and more robustly than nucleus accumbens. *Nat Commun* **9**:4350.

Pnevmatikakis EA, Giovannucci A. 2017. NoRMCorre: An online algorithm for piecewise rigid motion correction of calcium imaging data. *J Neurosci Methods* **291**:83–94.

Pnevmatikakis EA, Soudry D, Gao Y, Machado TA, Merel J, Pfau D, Reardon T, Mu Y, Lacefield C, Yang W, Ahrens M, Bruno R, Jessell TM, Peterka DS, Yuste R, Paninski L. 2016. Simultaneous Denoising, Deconvolution, and Demixing of Calcium Imaging Data. *Neuron* **89**:285–299.

Recanatesi S, Ocker GK, Buice MA, Shea-Brown E. 2019. Dimensionality in recurrent spiking networks: Global trends in activity and local origins in connectivity. *PLoS Comput Biol* **15**:e1006446.

Rescorla RA. 1972. A theory of Pavlovian conditioning : Variations in the effectiveness of reinforcement and non-reinforcement. *Classical conditioning, Current research and theory* **2**:64–69.

Ricardo JA. 1980. Efferent connections of the subthalamic region in the rat. I. The subthalamic nucleus of Luys. *Brain Res* **202**:257–271.

Richard JM, Ambroggi F, Janak PH, Fields HL. 2016. Ventral Pallidum Neurons Encode Incentive Value and Promote Cue-Elicited Instrumental Actions. *Neuron* **90**:1165–1173.

Schultz W, Dayan P, Montague PR. 1997. A neural substrate of prediction and reward. *Science* **275**:1593–1599.

Scott JW. 1981. Electrophysiological identification of mitral and tufted cells and distributions of their axons in olfactory system of the rat. *J Neurophysiol* **46**:918–931.

Shannon CE. 1948. A mathematical theory of communication. *The Bell System Technical Journal* **27**:379–423.

Smith KS, Tindell AJ, Aldridge JW, Berridge KC. 2009. Ventral pallidum roles in reward and motivation. *Behav Brain Res* **196**:155–167.

Soares-Cunha C, de Vasconcelos NAP, Coimbra B, Domingues AV, Silva JM, Loureiro-Campos E, Gaspar R, Sotiropoulos I, Sousa N, Rodrigues AJ. 2020. Nucleus accumbens medium spiny neurons subtypes signal both reward and aversion. *Mol Psychiatry* **25**:3241–3255.

Stephenson-Jones M, Bravo-Rivera C, Ahrens S, Furlan A, Xiao X, Fernandes-Henriques C, Li B. 2020. Opposing Contributions of GABAergic and Glutamatergic Ventral Pallidal Neurons to Motivational Behaviors. *Neuron* **105**:921–933.e5.

Sutton RS. 1988. Learning to predict by the methods of temporal differences. *Mach Learn* **3**:9–44.

Tachibana Y, Hikosaka O. 2012. The primate ventral pallidum encodes expected reward value and regulates motor action. *Neuron* **76**:826–837.

Tindell AJ, Smith KS, Berridge KC, Aldridge JW. 2005. VP neurons integrate learning and physiological signals to code incentive salience of conditioned cues. *Soc Neurosci Abstr*.

Tindell AJ, Smith KS, Peciña S, Berridge KC, Aldridge JW. 2006. Ventral pallidum firing codes hedonic reward: when a bad taste turns good. *J Neurophysiol* **96**:2399–2409.

Tritsch NX, Sabatini BL. 2012. Dopaminergic modulation of synaptic transmission in cortex and striatum. *Neuron* **76**:33–50.

Turner MS, Lavin A, Grace AA, Napier TC. 2001. Regulation of limbic information outflow by the subthalamic nucleus: excitatory amino acid projections to the ventral pallidum. *J Neurosci* **21**:2820–2832.

Wang PY, Boboila C, Chin M, Higashi-Howard A, Shamash P, Wu Z, Stein NP, Abbott LF, Axel R. 2020. Transient and Persistent Representations of Odor Value in Prefrontal Cortex. *Neuron* **108**:209–224.e6.

Watabe-Uchida M, Zhu L, Ogawa SK, Vamanrao A, Uchida N. 2012. Whole-brain mapping of direct inputs to midbrain dopamine neurons. *Neuron* **74**:858–873.

1013 Wesson DW. 2020. The Tubular Striatum. *J Neurosci* **40**:7379–7386.
1014 Wesson DW, Wilson DA. 2010. Smelling Sounds: Olfactory–Auditory Sensory Convergence in
1015 the Olfactory Tubercle. *J Neurosci* **30**:3013–3021.
1016 Wieland S, Schindler S, Huber C, Köhr G, Oswald MJ, Kelsch W. 2015. Phasic Dopamine
1017 Modifies Sensory-Driven Output of Striatal Neurons through Synaptic Plasticity. *J Neurosci*
1018 **35**:9946–9956.
1019 Zahm DS, Heimer L. 1987. The ventral striatopallidothalamic projection. III. Striatal cells of the
1020 olfactory tubercle establish direct synaptic contact with ventral pallidal cells projecting to
1021 mediodorsal thalamus. *Brain Res* **404**:327–331.
1022 Zhang Z, Liu Q, Wen P, Zhang J, Rao X, Zhou Z, Zhang H, He X, Li J, Zhou Z, Xu X, Zhang X,
1023 Luo R, Lv G, Li H, Cao P, Wang L, Xu F. 2017a. Activation of the dopaminergic pathway
1024 from VTA to the medial olfactory tubercle generates odor-preference and reward. *Elife* **6**.
1025 doi:10.7554/eLife.25423
1026 Zhang Z, Zhang H, Wen P, Zhu X, Wang L, Liu Q, Wang J, He X, Wang H, Xu F. 2017b. Whole-
1027 Brain Mapping of the Inputs and Outputs of the Medial Part of the Olfactory Tubercle. *Front*
1028 *Neural Circuits* **11**:52.
1029 Zhou L, Furuta T, Kaneko T. 2003. Chemical organization of projection neurons in the rat
1030 accumbens nucleus and olfactory tubercle. *Neuroscience* **120**:783–798.

1031

Figure 1:

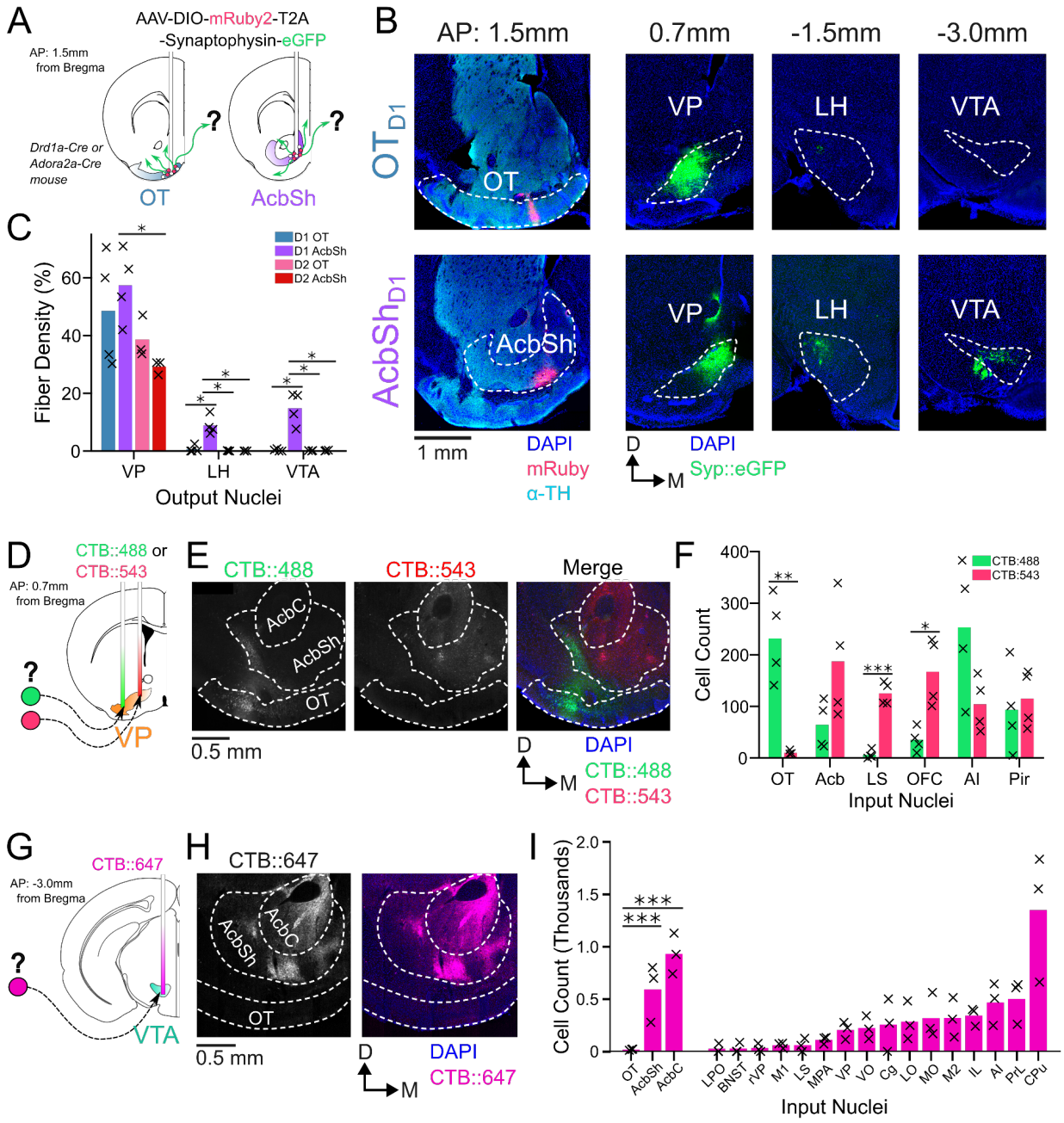
A
AAV-DIO-mRuby2-T2A
-Synaptophysin-eGFP
AP: 1.5mm
from Bregma
Drd1a-Cre or
Adora2a-Cre
mouse
OT
AcbSh
B
AP: 1.5mm
0.7mm
-1.5mm
-3.0mm
OT D1
AcbSh D1
OT
VP
LH
VTA
AcbSh
1 mm
DAPI
mRuby
α-TH
D
M
DAPI
Syp::eGFP
C
D1 OT
D1 AcbSh
D2 OT
D2 AcbSh
Fiber Density (%)
Output Nuclei
D
CTB::488 or
CTB::543
AP: 0.7mm
from Bregma
VP
E
CTB::488
CTB::543
Merge
AcbC
AcbSh
OT
0.5 mm
DAPI
CTB::488
CTB::543
F
CTB:488
CTB:543
Cell Count
OT
Acb
LS
OFC
AI
Pir
Input Nuclei
G
CTB::647
AP: -3.0mm
from Bregma
VTA
H
CTB::647
AcbSh
AcbC
OT
0.5 mm
DAPI
CTB::647
I
Cell Count (Thousands)
OT
AcbSh
AcbC
LPO
BNST
rVP
M1
LS
MPA
VP
VO
Cg
LO
MO
M2
IL
AI
PrL
CPu
Input Nuclei

Figure 1. OT_{D1} and OT_{D2} primarily project to the lateral portion of the VP. (**A**) Schematic representation of Cre-dependent anterograde axonal AAV tracing experiments used to characterize outputs of OT neurons. *Drd1*+ and *Drd2*+ neurons were separately labeled by using *Drd1*-Cre and *Adora2a*-Cre mouse lines, respectively. (**B**) Representative images from OT_{D1} (top) vs. the $AcbSh_{D1}$ injection (bot). Target sites (far-left column) are stained with α-tyrosine hydroxylase antibodies to visualize the boundary between VP and OT. (**C**) Quantifying the % of output regions with fluorescence (n=3-4). (**D**) Schematic representation of 2-color retrograde CTB tracing experiment used to confirm OT to VP connectivity. CTB::488 and CTB::543 were injected to the lateral and medial portion of the VP, respectively. (**E**) Representative images of CTB labeled neurons in the OT and Acb. (**F**) The number of labeled cells was quantified (n=4). (**G**) Schematic representation of retrograde CTB tracing experiment used to test OT to VTA connectivity. CTB::647 was injected in the VTA. (**H**) Representative image shows robust AcbSh and AcbC labeling but no OT labeling. (**I**) Quantification of labeling in different nuclei (n=3). Two-way ANOVAs followed by post-hoc t-tests for each output region were performed to generate p-values, which were then corrected for FDR by Benjamini-Hocherg procedure. ***$p<0.001$, **$p<0.01$, *$p<0.05$.

Figure 2:

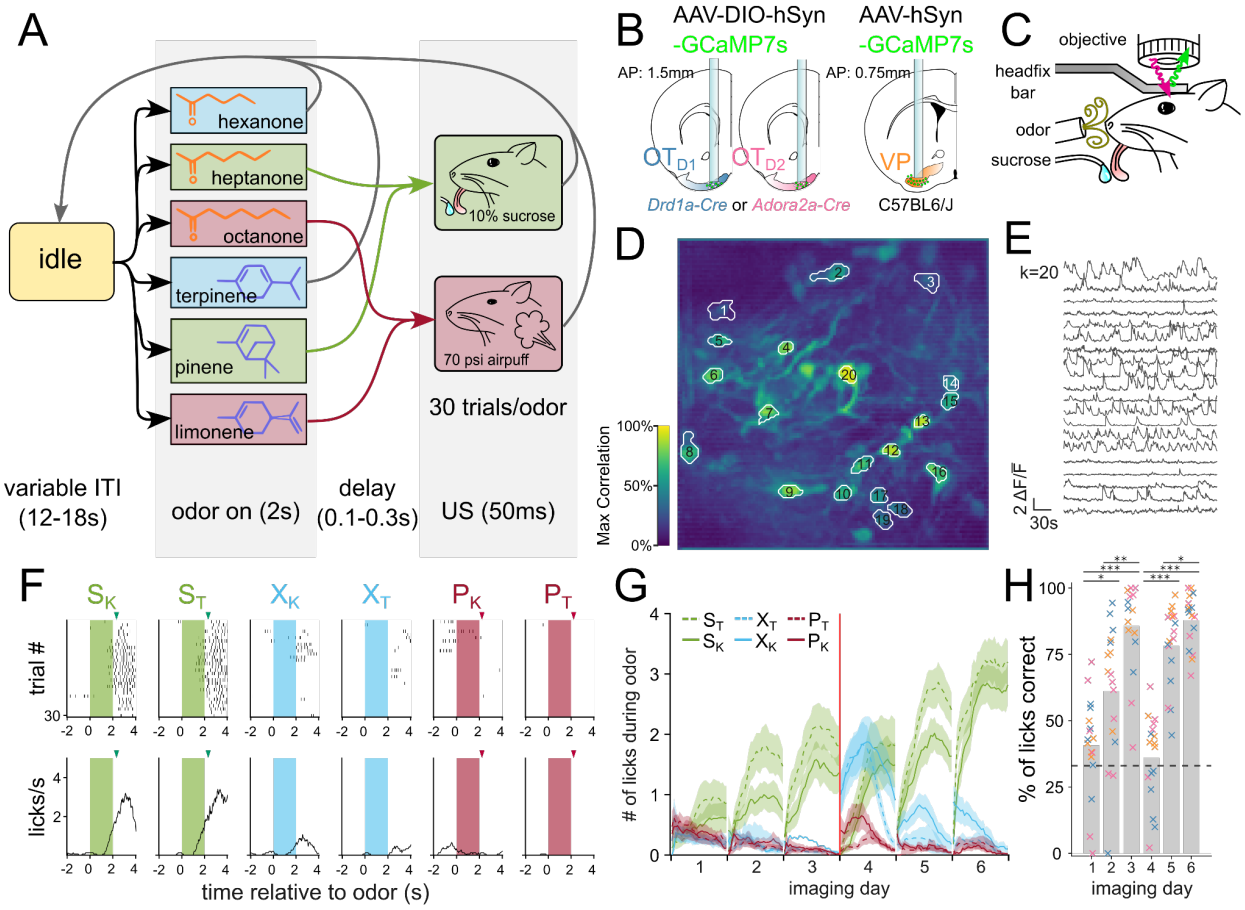
A
hexanone
heptanone
octanone
terpinene
pinene
limonene
idle
10% sucrose
70 psi airpuff
30 trials/odor
variable ITI
(12-18s)
odor on (2s)
delay
(0.1-0.3s)
US (50ms)
B
AAV-DIO-hSyn
-GCaMP7s
AAV-hSyn
-GCaMP7s
AP: 1.5mm
AP: 0.75mm
OT D1
OT D2
VP
Drd1a-Cre or Adora2a-Cre
C57BL6/J
C
objective
headfix
bar
odor
sucrose
D
Max Correlation
100%
50%
0%
E
k=20
2 ΔF/F
30s
F
S K
S T
X K
X T
P K
P T
trial #
licks/s
time relative to odor (s)
G
# of licks during odor
imaging day
H
% of licks correct
imaging day

Figure 2. Head-fixed 2-photon Ca^{2+} imaging of OT_{D1}, OT_{D2}, or VP neurons during 6-odor conditioning paradigm. (**A**) State-diagram of odor conditioning paradigm. Each trial begins with 2 seconds of odor delivery. Odors are chosen in pseudorandomized order such that the same odor is not repeated more than twice in a row. At the end of odor delivery, there is a variable delay (100-300ms), after which the animal is given either a 10% sucrose solution (S_K and S_T), a 70 psi airpuff (P_K and P_T), or nothing (X_K and X_T). Trials are separated by a variable intertrial interval (ITI; 12-18s). Schematic representation of (**B**) lens implant surgery and (**C**) headfix 2-photon microscopy setup. An example of spatial (**D**) and temporal (**E**) components extracted by CNMF from *Drd1*-Cre animal on day 3 of imaging. (**D**) The spatial footprints of 20 example neurons are shown on top of a maximum-correlation pixel image that was used to seed the factorization. The number displayed over each neuron matches the row number of the temporal components in (**E**). (**F**) An example raster plot (top) and averaged-across-trials trace (bottom) of the licking behavior recorded concurrently as (**D**) and (**E**). The timing of odor delivery is shown as shaded rectangles. The timing of US delivery is shown as arrowheads. (**G**) The mean total licks during each of the odors is shown averaged across all animals (n=17) after application of a moving-average filter with a window size of 10 trials. Red line marks the sucrose and airpuff contingency switch between day 3 and day 4. (**H**) Bar graph showing the ratio of licks during either S_K or S_T to licks during any odor. The effects of imaging day and lens target site were analyzed using a 2-way ANOVA. The imaging day, but not lens target site, was a significant factor on licking accuracy (F_{day}=27.64 vs. $F_{lens\ location}$=2.30).

Figure 3:

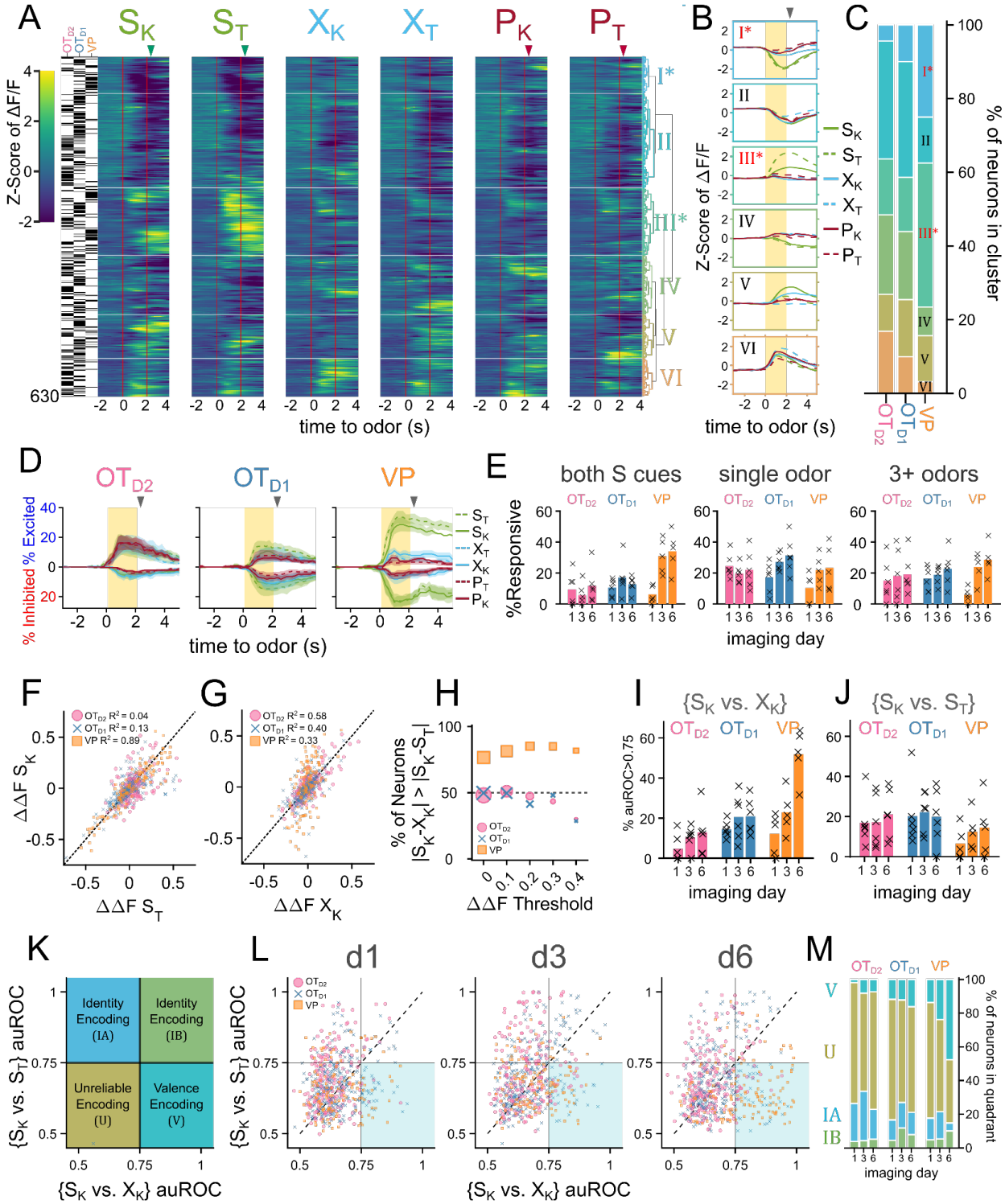
A
B
C
D
E
F
G
H
I
J
K
L
M
Z-Score of ΔF/F
time to odor (s)
% of neurons in cluster
% Inhibited % Excited
both S cues
single odor
3+ odors
%Responsive
imaging day
ΔΔF S_K
ΔΔF S_T
ΔΔF X_K
% of Neurons
ΔΔF Threshold
{S_K vs. X_K}
{S_K vs. S_T}
% auROC>0.75
Identity Encoding (IA)
Identity Encoding (IB)
Unreliable Encoding (U)
Valence Encoding (V)
d1
d3
d6
% of neurons in quadrant

Figure 3. VP neurons encode reward-contingency more robustly than OT_{D1} or OT_{D2} neurons. (**A**) Heatmap of odor-evoked activities in OT_{D1}, OT_{D2}, and VP neurons from day 6 of imaging. The fluorescence measurements from each neuron were averaged over trials, Z-scored, then pooled for hierarchical clustering. Neurons are grouped by similarity, with the dendrogram shown on the right and a raster plot on the left indicating which region a given neuron is from. Horizontal white lines demarcate the boundaries between the 6 clusters. Odor delivered at 0-2 seconds marked by vertical red lines and US delivery is marked by arrowheads. From left to right, the columns represent neural responses to sucrose-paired ketone and terpene, control ketone and terpene, and airpuff-paired ketone and terpene (S_K, S_T, X_K, X_T, P_K, P_T). (**B**) Average Z-scored activity of each cluster to each of the 6 odors on day 6 of imaging. Yellow bar indicates 2-seconds of odor exposure. (**C**) The distribution of clusters by population. (**D**) Percentage of total neurons that were significantly excited or inhibited by each odor (Bonferroni-adjusted FDR < 0.05) as a function of time relative to odor. Bar represents the mean across biological replicates and x's mark individual animals. (**E**) Bar graph showing % of neurons from each population that are responsive to both sucrose-paired odors in the same direction (left), responsive to only a single odor (middle), or responsive to at least 3 odors (right). (**F**) Scatterplot comparing the magnitudes of S_K responses ($\Delta\Delta S_K$) to S_T responses ($\Delta\Delta S_T$). The dotted line represents the hypothetical scenario where $\Delta\Delta S_K = \Delta\Delta S_T$. For each population, the R^2 value of the 2-d distribution compared to the $\Delta\Delta S_K = \Delta\Delta S_T$ line is reported. (**G**) Same as F but comparing $\Delta\Delta S_K$ to $\Delta\Delta X_K$. (**H**) Lineplot showing the % of neurons from each population where the difference between $\Delta\Delta S_K$ and $\Delta\Delta X_K$ is lower than that between $\Delta\Delta S_K$ and $\Delta\Delta S_T$. (**I**) Bargraph showing % of neurons whose responses to {S_K vs. X_K} can be discriminated by a linear classifier with auROC>0.75. (**J**) Same as H but for {S_K vs S_T}. (**K**) Schematic representation of 4 possible categories for a joint-distribution of {S_K vs. X_K} and {S_K vs. S_T} auROC values. Identity-encoding neurons could be in any quadrant other than the bottom-left whereas valence-encoding neurons should be in the bottom-right quadrant. (**L**) Scatterplot of each neuron's auROC value for {S_K vs. X_K} on the x-axis and {S_K vs. S_T} on the y-axis on days 1, 3 and 6 of imaging. (**M**) Stacked bar graph showing the distribution of neurons from each population that fall into each of the 4 quadrants across the 3 different imaging days.

Figure 4:

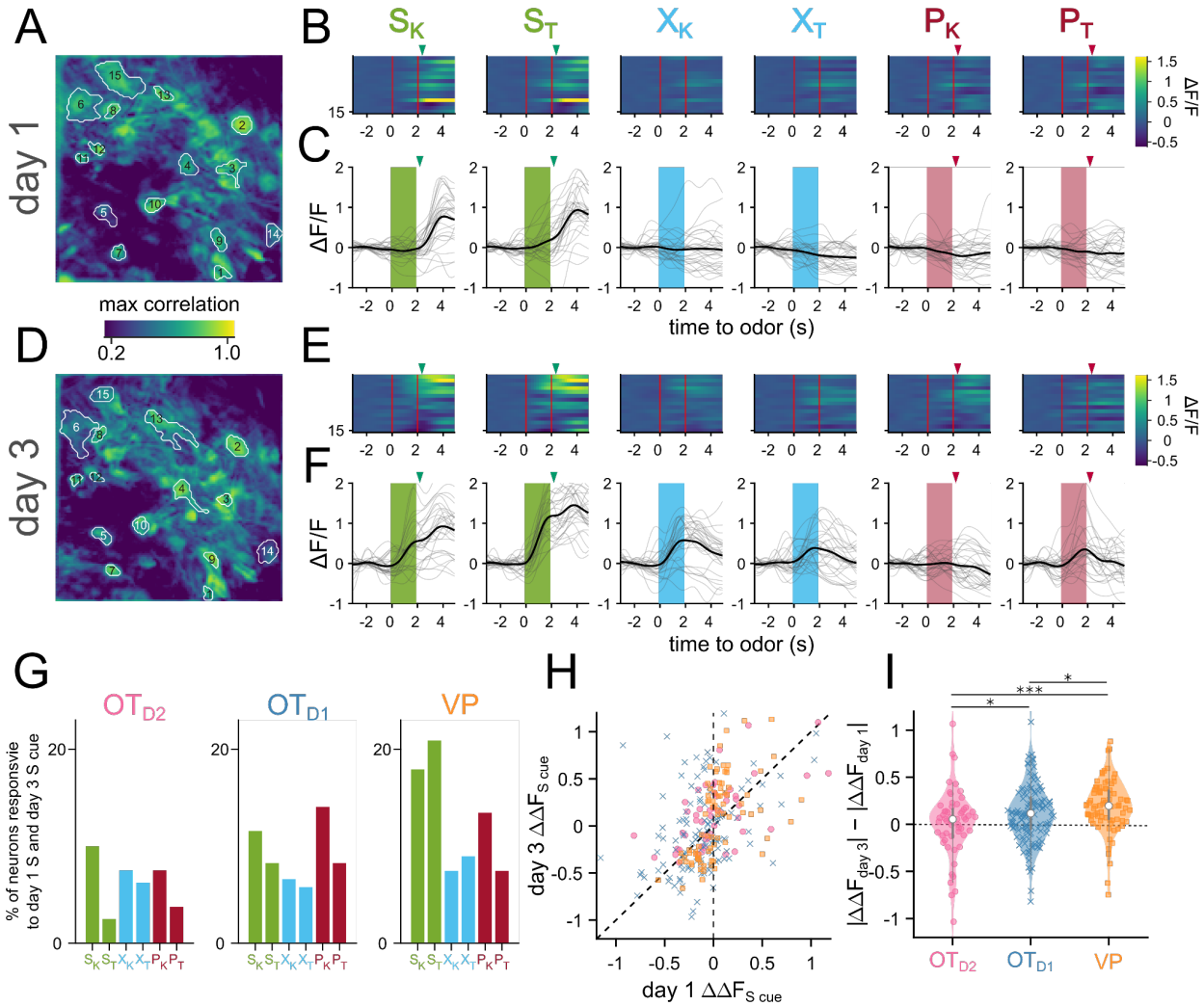
A
day 1
max correlation
0.2
1.0
B
C
D
day 3
E
F
ΔF/F
time to odor (s)
G
% of neurons responsvie to day 1 S and day 3 S cue
OTD2
OTD1
VP
H
day 3 ΔΔF S cue
day 1 ΔΔF S cue
I
|ΔΔF day 3| − |ΔΔF day 1|

Figure 4. Sucrose responsive VP neurons become sucrose-cue responsive after pairing. (**A**) The spatial footprints of 15 neurons from day 1 are outlined over a max-correlation projection image. (**B**) Heatmap of averaged-over-trials ΔF/F in response to 6 odors on day 1. Odor delivery period is shown with 2 red vertical lines and sucrose/airpuff timing is shown with downward arrowhead. (**C**) An example neuron's responses on day 1 across 30 trials to 6 different odors. Individual trial traces are shown in light gray whereas the averaged-across trials trace is shown in black. Odor delivery period is depicted as shaded rectangles and US delivery is marked by arrowheads. (**D-F**) Same as (**A-C**), respectively, but for day 3. (**G**) Percentage of all tracked neurons that were both sucrose-responsive on day 1 and odor-responsive in the same direction on day 3. (**H**) Scatter plot of averaged-over-trials responses to S_K or S_T on day 1 (x-axis) and day 3 (y-axis). Each point is a neuron that was successfully matched from day 1 and day 3. Neurons from OT_{D2}, OT_{D1}, and VP are plotted as pink circles, blue crosses, and yellow squares, respectively. Neurons that have increased response magnitudes on day 3 would fall between the 2 dotted lines. (**I**) Violin plot showing the distributions of day 3 responsive magnitude - day 1 response magnitude.

Figure 5:

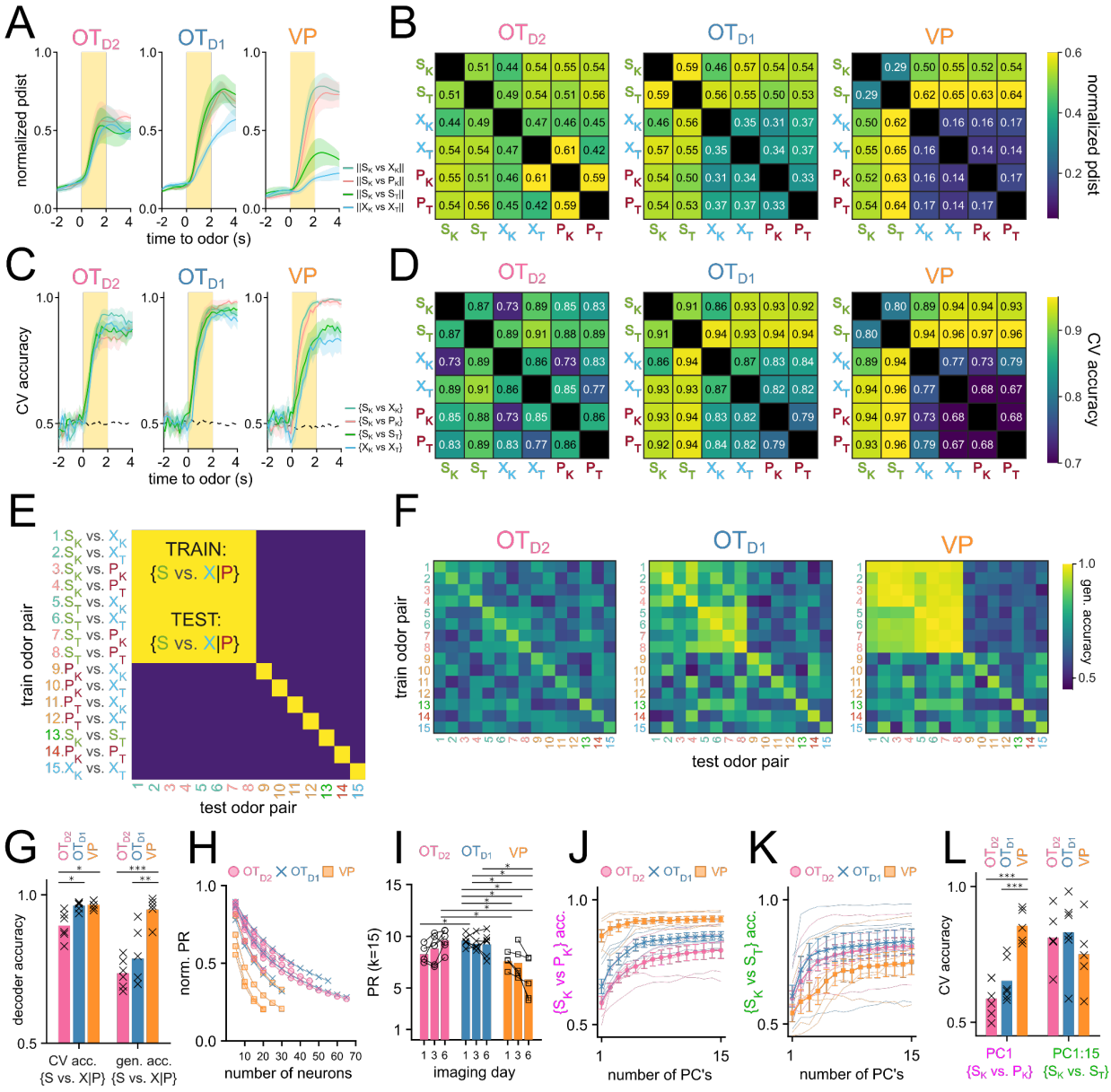
A
OTD2
OTD1
VP
normalized pdist
time to odor (s)
	SK vs XK	
	SK vs PK	
	SK vs ST	
	XK vs XT	
B
normalized pdist
C
CV accuracy
time to odor (s)
{SK vs XK}
{SK vs PK}
{SK vs ST}
{XK vs XT}
D
CV accuracy
E
TRAIN:
{S vs. X|P}
TEST:
{S vs. X|P}
train odor pair
test odor pair
F
train odor pair
test odor pair
gen. accuracy
G
decoder accuracy
CV acc.
{S vs. X|P}
gen. acc.
{S vs. X|P}
H
norm. PR
number of neurons
I
PR (k=15)
imaging day
J
{SK vs PK} acc.
number of PC's
K
{SK vs ST} acc.
number of PC's
L
CV accuracy
PC1
{SK vs. PK}
PC1:15
{SK vs. ST}

Figure 5. OT encodes odor identity in high-dimensional space and VP encodes reward-contingency in low-dimensional space. (**A**) Average normalized pairwise euclidean distance between odor-evoked population-level activity from day 6 of imaging shown as a function of time relative to odor delivery. Traces show the average value across biological replicates of the same population and the shaded areas represent the average ± SEM. (**B**) A heatmap of the average normalized pairwise distance during the odor delivery period. (**C**) Average CV accuracy of binary pairwise linear classifiers trained on population data plotted against time relative to odor delivery. (**D**). A heatmap of the average CV accuracy during the odor delivery period. (**E**) Schematic representation of generalized linear classification performance for an idealized valence encoder. Each row corresponds to the training odor-pair and each column corresponds to the testing odor-pair. For an idealized valence encoder, the decodability would generalize well across odor-pairs of the equal valence grouping outlined in red. Note that the elements along the diagonal are cases where training and testing odor-pairs are identical and do not reflect generalizability. (**F**) Heatmap representing the maximum generalized linear classification accuracy during odor delivery period averaged across biological replicates for each population. (**G**) Maximum cross validated linear classifier accuracy for S_K vs. X_K (trained on S_K vs. X_K) and the generalized accuracy for S_K vs. X_K after training on S_T vs X_T. (**H**) Average PR normalized to *n* calculated after randomly subsampling an increasing number of neurons. (**I**) Average PR calculated after subsampling 15 neurons. (**J**) Average CV accuracy of linear classifiers trained on {S_K vs. P_K}. For each simultaneously imaged group of neurons, 15 neurons were subsampled and classifiers were trained on an increasing number of principal components. The average across subsampling is reported. (**K**) Average CV accuracy of linear classifiers trained on {S_K vs. S_T}. (**L**) Comparison of the average accuracy of {S_K vs. P_K} classifiers trained on the 1st PC vs. {S_K vs. S_T} classifiers trained on all 15 PC's.

Figure 6:

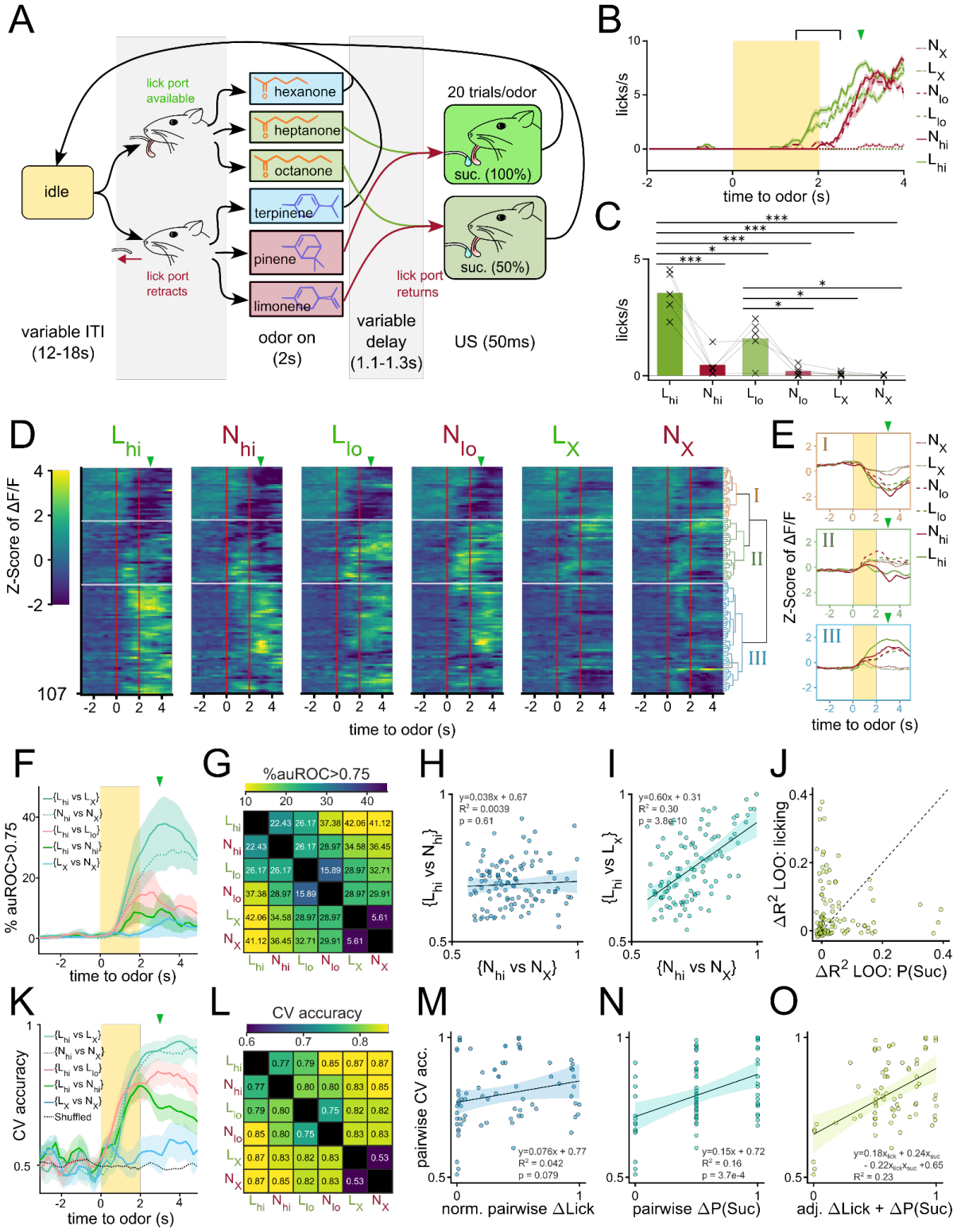
A
idle
lick port available
lick port retracts
hexanone
heptanone
octanone
terpinene
pinene
limonene
20 trials/odor
suc. (100%)
suc. (50%)
lick port returns
variable ITI (12-18s)
odor on (2s)
variable delay (1.1-1.3s)
US (50ms)
B
licks/s
time to odor (s)
C
licks/s
D
Z-Score of ΔF/F
time to odor (s)
E
Z-Score of ΔF/F
time to odor (s)
F
% auROC>0.75
time to odor (s)
G
%auROC>0.75
H
y=0.038x + 0.67
R² = 0.0039
p = 0.61
I
y=0.60x + 0.31
R² = 0.30
p = 3.8e-10
J
ΔR² LOO: licking
ΔR² LOO: P(Suc)
K
CV accuracy
time to odor (s)
L
CV accuracy
M
pairwise CV acc.
y=0.076x + 0.77
R² = 0.042
p = 0.079
norm. pairwise ΔLick
N
y=0.15x + 0.72
R² = 0.16
p = 3.7e-4
pairwise ΔP(Suc)
O
y=0.18x_lick + 0.24x_suc - 0.22x_lick x_suc +0.65
R² = 0.23
adj. ΔLick + ΔP(Suc)

Figure 6. Separate VP populations encode reward-contingency and licking vigor.
(**A**) State diagram for odor pairing paradigm where lick spout is removed during the presentation of half of the odors. The paradigm is similar to one described in Fig2A with the following key differences: 1) the lick spout is moved away from the animal's mouth during the presentation of half of the odors (N_{hi}, N_{lo}, N_X). 2) sucrose is delivered after a longer variable delay (1.1-1.3s). 3) 2 of the odors have 100% sucrose contingency (L_{hi}, N_{hi}), 2 of the odors have 50% sucrose contingency (L_{lo}, N_{lo}), and the other 2 have 0% sucrose contingency (L_X, N_X). (**B**) Licking behavior to 6 odors averaged across 30 trials from a representative animal. Duration of odor delivery is marked by the shaded rectangle and the average time of sucrose delivery is marked by the arrowhead. The time bin used for subsequent analysis (last 0.5s of odor and first 0.5s of delay) is outlined by square brackets (**C**) Average licks/s for each odor measured between the last 0.5s of odor and the first 0.5s of delay. Data were pooled from the day of highest difference between licks to L_{hi} and N_{hi}. The effect of lick spout presence and sucrose contingency were analyzed using a 2-way ANOVA followed by post-hoc t-tests were performed to generate p-values. These values were then corrected for FDR by the Benjamini-Hocherg procedure. □□□p<0.001, □□p<0.01, □p<0.05. (**D**) Heatmap of odor-evoked activity in VP neurons pooled from each animal's day of highest difference between licks to L_{hi} and N_{hi}. Neurons are grouped according to the clustering dendrogram, shown on the right. Horizontal white lines demarcate the boundaries between the 3 clusters. Odor delivery is marked by vertical red lines. (**E**) Average Z-scored activity of each cluster to each of the 6 odors. Yellow bar indicates 2-seconds of odor exposure. (**F**) The percentage of single-neuron linear classifiers with auROC>0.75 as a function of time relative to odor delivery. Shaded area represents the SEM across biological replicates (n=5). (**G**) Heatmap of the percentage of pooled VP neurons with auROC>0.75 during the last 0.5s of odor and first 0.5s of delay. (**H**) Scatterplot comparing the auROC for {L_{hi} vs N_{hi}} (y-axis) and {N_{hi} vs. N_X} (x-axis) for each neuron. The line of best fit is plotted as a dotted line, with the 95% confidence interval shaded in. (**I**) Same as (H) but comparing the auROC for {L_{hi} vs L_X} (y-axis) and {N_{hi} vs. N_X} (x-axis). (**J**) Scatterplot comparing regression models that explain each neuron's activity on a given trial as a function of anticipatory licking or sucrose contingency. The values plotted are the loss in R^2 in models without anticipatory licking (y-axis) or sucrose contingency (x-axis) when compared to a model with both variables and their interaction term. (**K**) CV accuracy for 5 different odor pairs as a function of time relative to odor delivery. (**L**) Heatmap of average pairwise CV accuracy trained on the last 0.5s of odor and the first 0.5s of delay. (**M**) Scatterplot of all pairwise classifier accuracies from all animals (y-axis) and the corresponding range-normalized average pairwise difference in anticipatory licking (x-axis). (**N**) Scatterplot of all pairwise classifier accuracies from all animals (y-axis) and the corresponding pairwise difference in reward-contingency (x-axis). (**O**) Scatterplot of all pairwise classifier accuracies (y-axis) and the adjusted combined model of ranged-normalized Δlick and Δreward-contingency (x-axis).

Figure S1:

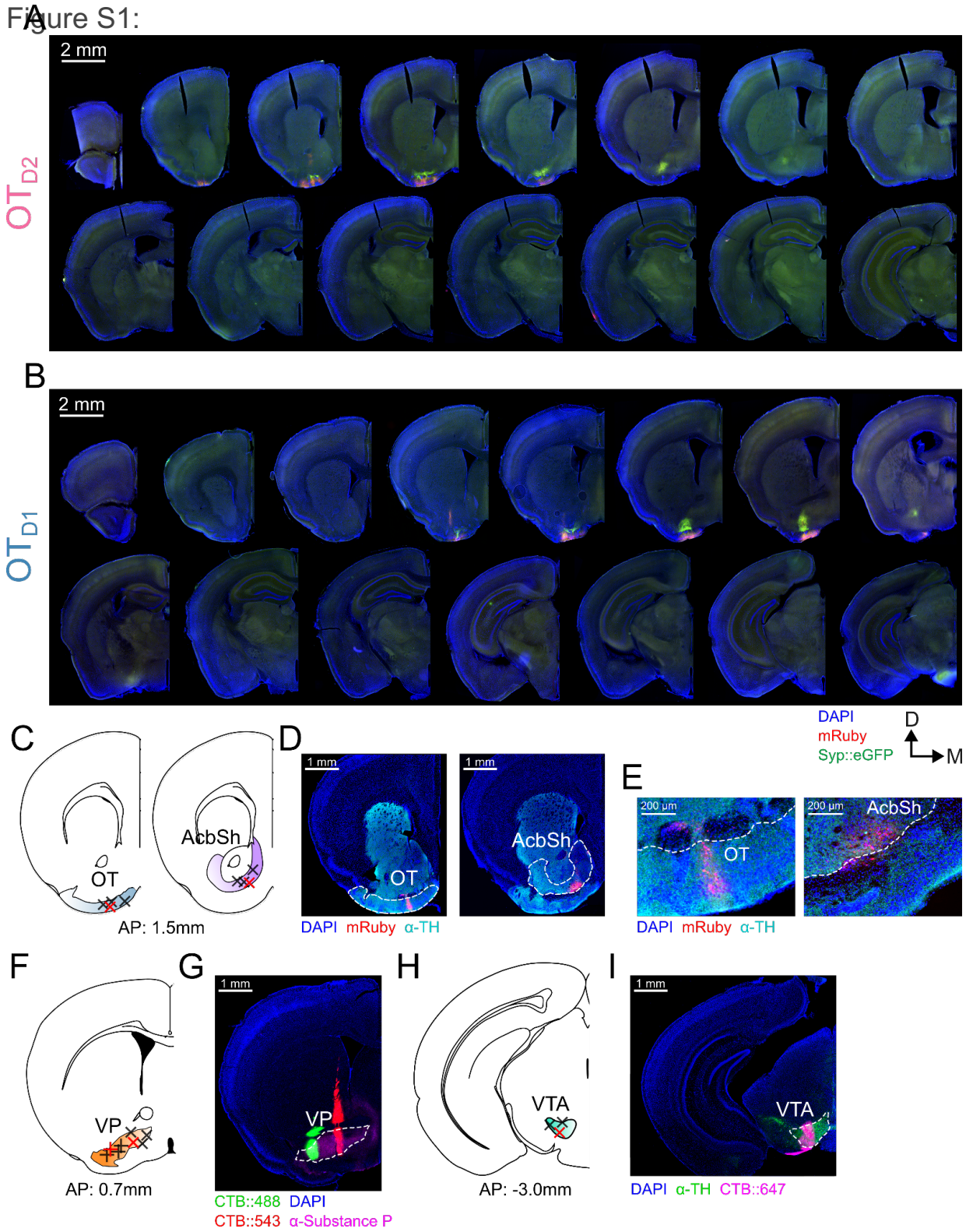
A
2 mm
OT D2
B
2 mm
OT D1
C
OT
AcbSh
AP: 1.5mm
D
1 mm
OT
1 mm
AcbSh
DAPI mRuby α-TH
DAPI
mRuby
Syp::eGFP
D
M
E
200 µm
OT
200 µm
AcbSh
DAPI mRuby α-TH
F
VP
AP: 0.7mm
G
1 mm
VP
CTB::488 DAPI
CTB::543 α-Substance P
H
VTA
AP: -3.0mm
I
1 mm
VTA
DAPI α-TH CTB::647

Figure S1. OT_{D1} and OT_{D2} primarily project to the lateral portion of the VP.
(**A**) Serial coronal sections from a representative experiment where AAVDJ-hSyn-FLEX-mRuby-T2A-syn-eGFP virus was injected into the anterior OT of an *Adora2a*-Cre mouse. Sections are roughly 400µm apart from each other and range from +2.5mm to -3.0mm relative to bregma. (**B**) Same as (A) but in a *Drd1*-Cre mouse. (**C**) Schematic showing the centroids of 4 injection sites for OT and AcbSh anterograde tracing experiments. (**D**, **E**) Representative images of the injection sites shown in (C). Sections were counterstained with α-TH to delineate the boundary between the striatum and the rostral ventral pallidum. The centroids of these samples are marked as red x's in (C). (**F**) Schematic showing the centroids of 4 CTB injection sites for lateral and medial VP. CTB::488 injection to the lateral VP are marked by +'s whereas CTB::543 injection to the medial VP are marked by x's. (**G**) Representative image of the injection sites shown in (F). Sections were counterstained with α-Substance P to mark the boundary of the VP. The centroids of this sample are marked by the red + and red x in (F). (**H**) Schematic showing the centroids of 3 CTB injection sites for VTA. (**I**) Representative image of the injection sites shown in (H). Sections were counterstained with α-TH to mark the boundary of the VTA.

Figure S2:

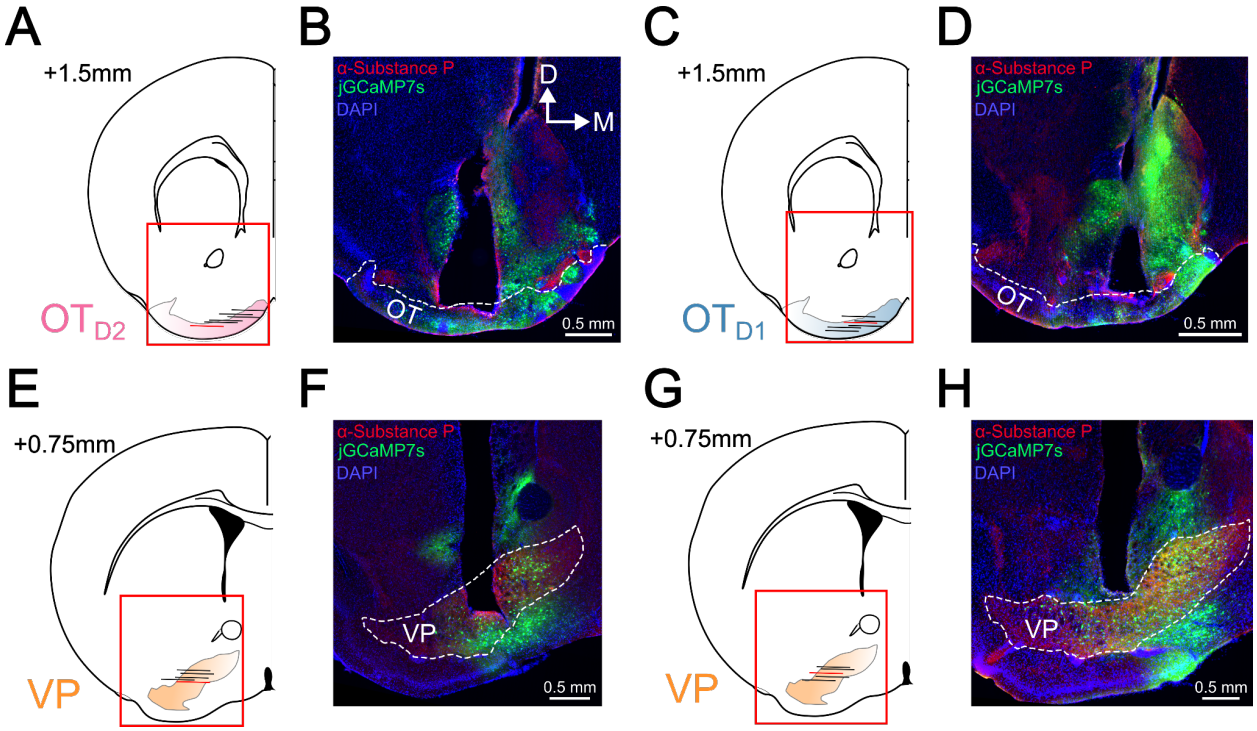
A
+1.5mm
OT$_{D2}$
B
α-Substance P
jGCaMP7s
DAPI
D
M
OT
0.5 mm
C
+1.5mm
OT$_{D1}$
D
α-Substance P
jGCaMP7s
DAPI
OT
0.5 mm
E
+0.75mm
VP
F
α-Substance P
jGCaMP7s
DAPI
VP
0.5 mm
G
+0.75mm
VP
H
α-Substance P
jGCaMP7s
DAPI
VP
0.5 mm

Figure S2 Histological verification of lens implant location.
(**A**) Schematic showing the center, along the AP axis, of the implanted GRIN lens in 6 OT_{D2} jGCaMP7s animals. (**B**) Representative image of lens implant sites shown in (A). Sections were counterstained with α-Substance P to delineate the boundary of the VP. This sample is marked by a red horizontal line in (A). (**C**) Schematic as in (A) for 6 OT_{D1} jGCaMP7s animals. (**D**) Representative image of lens implant sites shown in (C). (**E**) Schematic as in (A) for 5 VP jGCaMP7s animals. (**F**) Representative image of lens implant sites shown in (E). (**G**) Schematic as in (A) for 5 VP jGCaMP7s animals recorded during the lick spout retraction paradigm (Figure 6). (**H**) Representative image of lens implant sites shown in (G). Sections were counterstained with α-Substance P to delineate the boundary of the VP. This sample is marked by a red horizontal line in (G).

Figure S3:

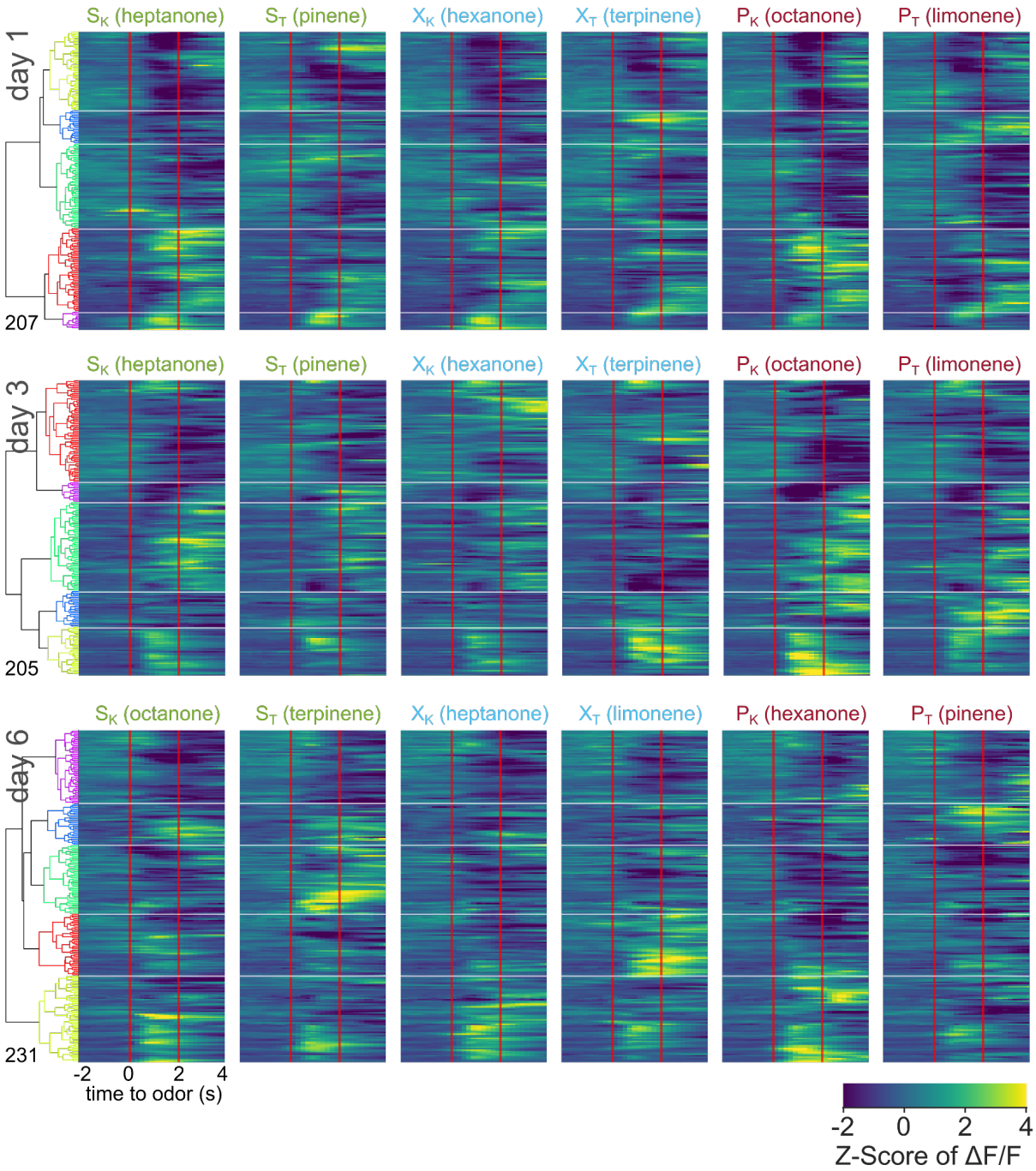
S_K (heptanone)
S_T (pinene)
X_K (hexanone)
X_T (terpinene)
P_K (octanone)
P_T (limonene)
day 1
207
S_K (heptanone)
S_T (pinene)
X_K (hexanone)
X_T (terpinene)
P_K (octanone)
P_T (limonene)
day 3
205
S_K (octanone)
S_T (terpinene)
X_K (heptanone)
X_T (limonene)
P_K (hexanone)
P_T (pinene)
day 6
231
-2 0 2 4
time to odor (s)
-2 0 2 4
Z-Score of ΔF/F

Figure S3. Pooled averaged-over-trials neural activity of all neurons from OT_{D2} animals across days. Heatmap of odor-evoked activity in OT_{D2} neurons from day 1, day 3, and day 6 of imaging. The fluorescence measurements from each neuron were averaged over trials, Z-scored, then pooled for hierarchical clustering. Neurons are grouped by similarity, with the dendrogram shown on the right. Horizontal white lines demarcate the boundaries between the 6 clusters. Odor delivered at 0-2 seconds marked by vertical red lines. From left to right, the columns represent neural responses to sucrose-paired ketone and terpene, control ketone and terpene, and airpuff-paired ketone and terpene (S_K, S_T, X_K, X_T, P_K, P_T). Data is pooled from 6 animals.

Figure S4:

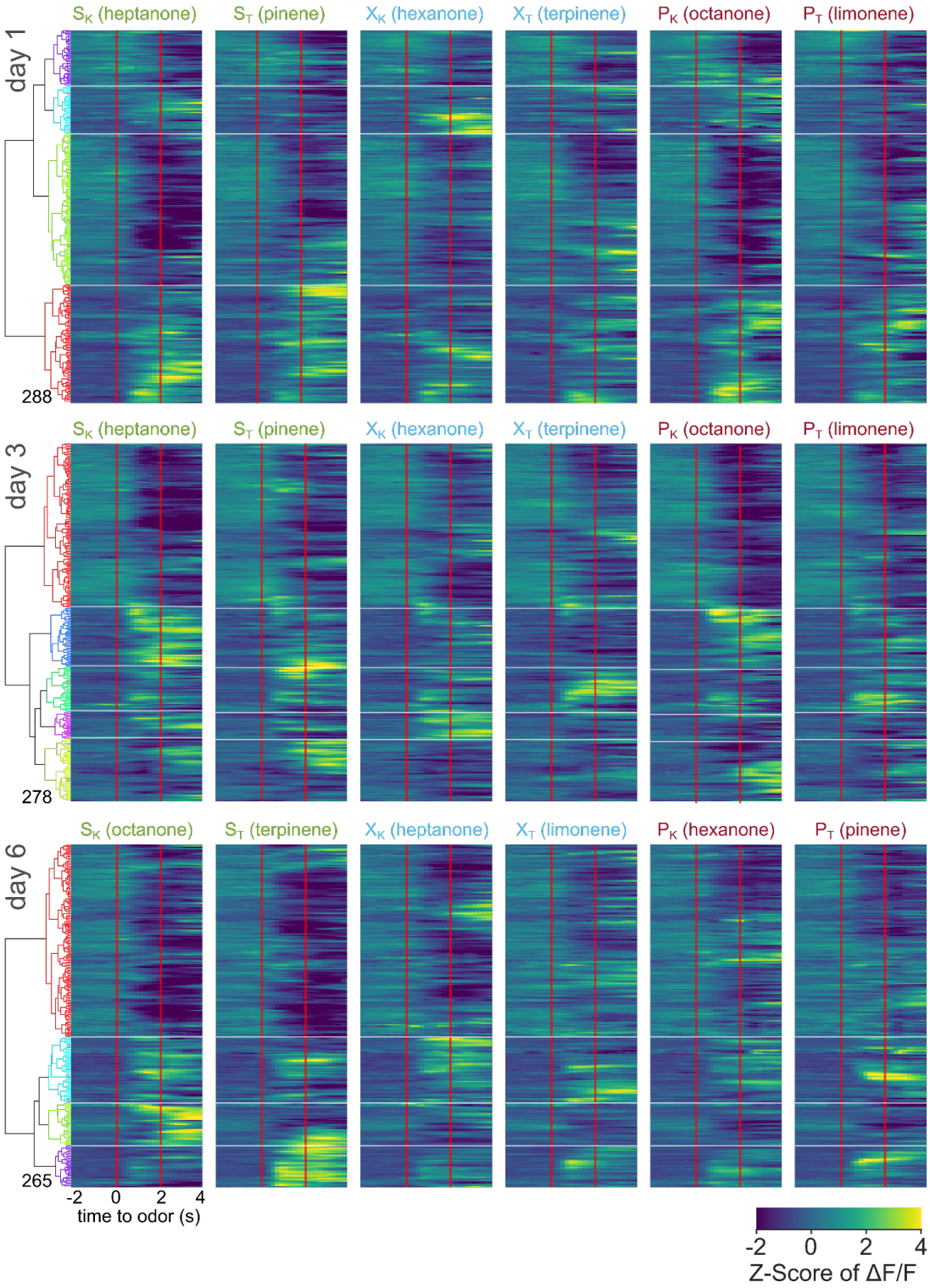
day 1
S_K (heptanone)
S_T (pinene)
X_K (hexanone)
X_T (terpinene)
P_K (octanone)
P_T (limonene)
288
day 3
S_K (heptanone)
S_T (pinene)
X_K (hexanone)
X_T (terpinene)
P_K (octanone)
P_T (limonene)
278
day 6
S_K (octanone)
S_T (terpinene)
X_K (heptanone)
X_T (limonene)
P_K (hexanone)
P_T (pinene)
265
-2 0 2 4
time to odor (s)
-2 0 2 4
Z-Score of ΔF/F

Figure S4. Pooled averaged-over-trials neural activity of all neurons from OT_{D1} animals across days. Heatmap of odor-evoked activity in OT_{D1} neurons from day 1, day 3, and day 6 of imaging.. The fluorescence measurements from each neuron were averaged over trials, Z-scored, then pooled for hierarchical clustering. Neurons are grouped by similarity, with the dendrogram shown on the right. Horizontal white lines demarcate the boundaries between the 6 clusters. Odor delivered at 0-2 seconds marked by vertical red lines. From left to right, the columns represent neural responses to sucrose-paired ketone and terpene, control ketone and terpene, and airpuff-paired ketone and terpene (S_K, S_T, X_K, X_T, P_K, P_T). Data is pooled from 6 animals.

Figure S5:

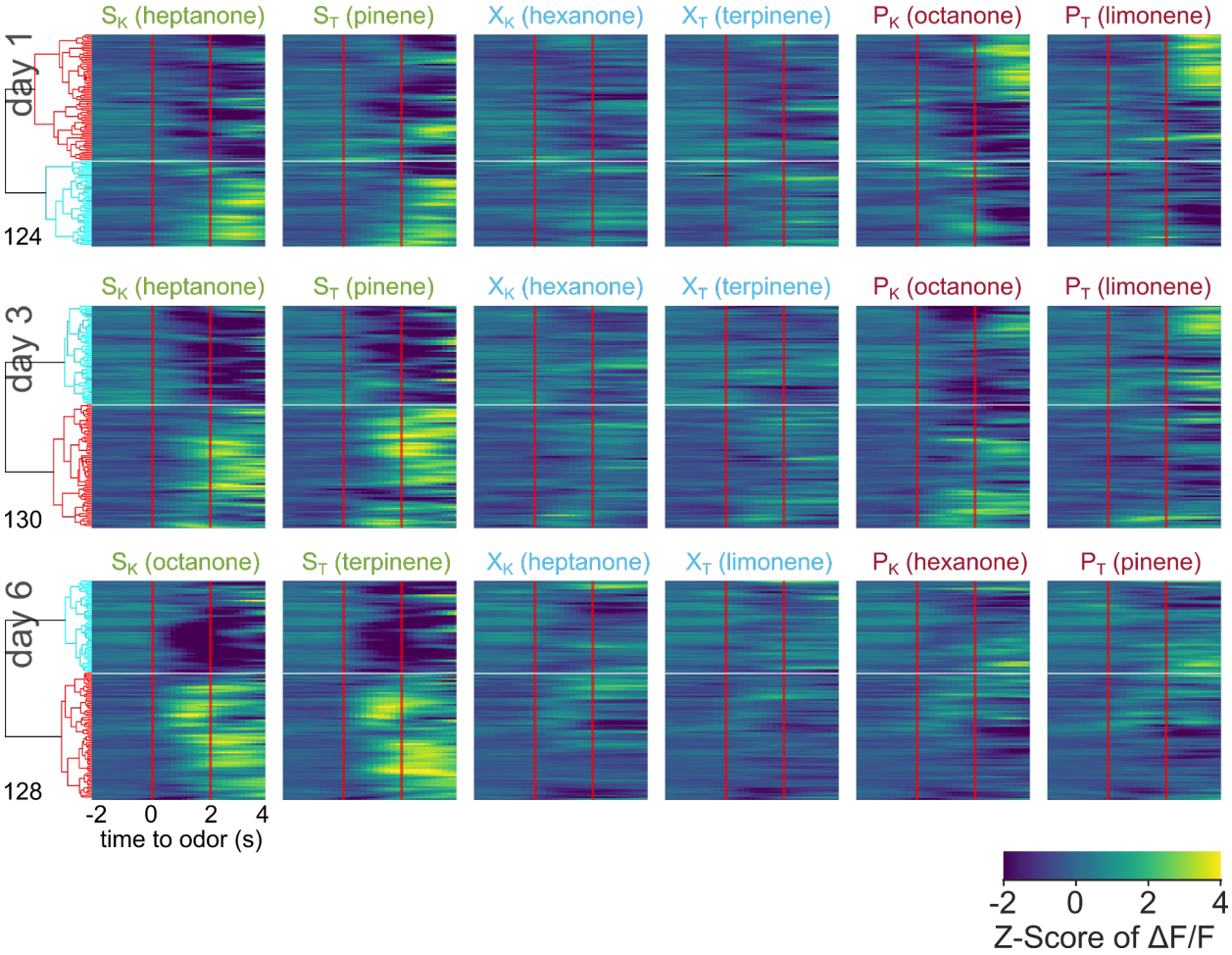
S_K (heptanone)
S_T (pinene)
X_K (hexanone)
X_T (terpinene)
P_K (octanone)
P_T (limonene)
day 1
124
S_K (heptanone)
S_T (pinene)
X_K (hexanone)
X_T (terpinene)
P_K (octanone)
P_T (limonene)
day 3
130
S_K (octanone)
S_T (terpinene)
X_K (heptanone)
X_T (limonene)
P_K (hexanone)
P_T (pinene)
day 6
128
-2 0 2 4
time to odor (s)
-2 0 2 4
Z-Score of ΔF/F

Figure S5. Pooled averaged-over-trials neural activity of all neurons from VP animals across days. Heatmap of odor-evoked activity in VP neurons from day 1, day 3, and day 6 of imaging. The fluorescence measurements from each neuron were averaged over trials, Z-scored, then pooled for hierarchical clustering. Neurons are grouped by similarity, with the dendrogram shown on the right. Horizontal white lines demarcate the boundaries between the 6 clusters. Odor delivered at 0-2 seconds marked by vertical red lines. From left to right, the columns represent neural responses to sucrose-paired ketone and terpene, control ketone and terpene, and airpuff-paired ketone and terpene (S_K, S_T, X_K, X_T, P_K, P_T). Data is pooled from 5 animals.

Figure S6:

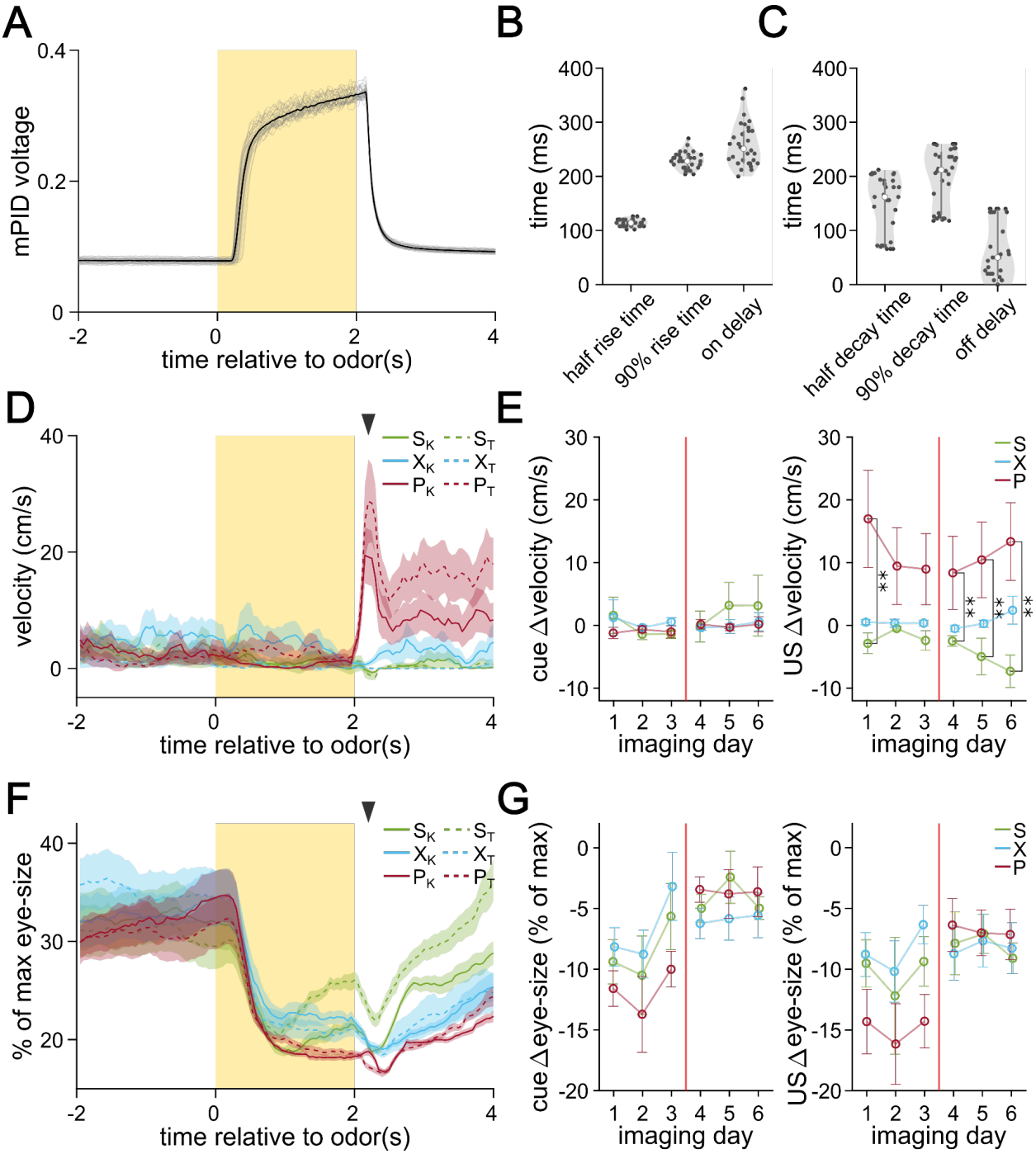
A
mPID voltage
0.4
0.2
0
-2
0
2
4
time relative to odor(s)
B
time (ms)
400
300
200
100
0
half rise time
90% rise time
on delay
C
time (ms)
half decay time
90% decay time
off delay
D
velocity (cm/s)
40
20
0
S_K
S_T
X_K
X_T
P_K
P_T
time relative to odor(s)
E
cue Δvelocity (cm/s)
US Δvelocity (cm/s)
30
20
10
0
-10
S
X
P
imaging day
1 2 3 4 5 6
F
% of max eye-size
40
30
20
time relative to odor(s)
G
cue Δeye-size (% of max)
US Δeye-size (% of max)
0
-5
-10
-15
-20
imaging day

Figure S6. Extended behavioral analysis from imaging period. (**A**) mPID voltage reading in response to 30 trials of odor (terpinene) delivery. The time period during which the odor valve was turned on is shown by the yellow rectangle. Individual recordings are shown in gray and the average is shown in black. (**B**) On-kinetics of odor delivery. On delay refers to the interval between the valve turning on and the mPID voltage increasing by more than 10% of baseline. (**C**) Off-kinetics of odor delivery. Off delay refers to the interval between the odor valve turning off and the mPID voltage decreasing by more than 10% of its maximum. (**D**) Representative velocity of the head-fixed mouse in response to the 6 different odors measured by a digital encoder. The lines represent the average across 30 trials and the shaded areas represent the SEM. The black arrowhead marks when the US is delivered. (**E**) The difference in walking velocity in response to odor (left) and US delivery (right). Differences are calculated between the last second before odor delivery and the last second before the odor exposure (left) or the first half second after US delivery (right) grouped by US pairing. Circles represent the average across animals and the error bars show SEM. (**F**) Representative changes in range-normalized eye-size in response to the 6 different odors. (**G**) The difference in eye-size in response to odor (left) and US delivery (right). Differences are calculated between the last second before odor delivery and the last second before the odor exposure (left) or the first half second after US delivery (right) grouped by US pairing. Circles represent the average across animals and the error bars show SEM.

Figure S7:

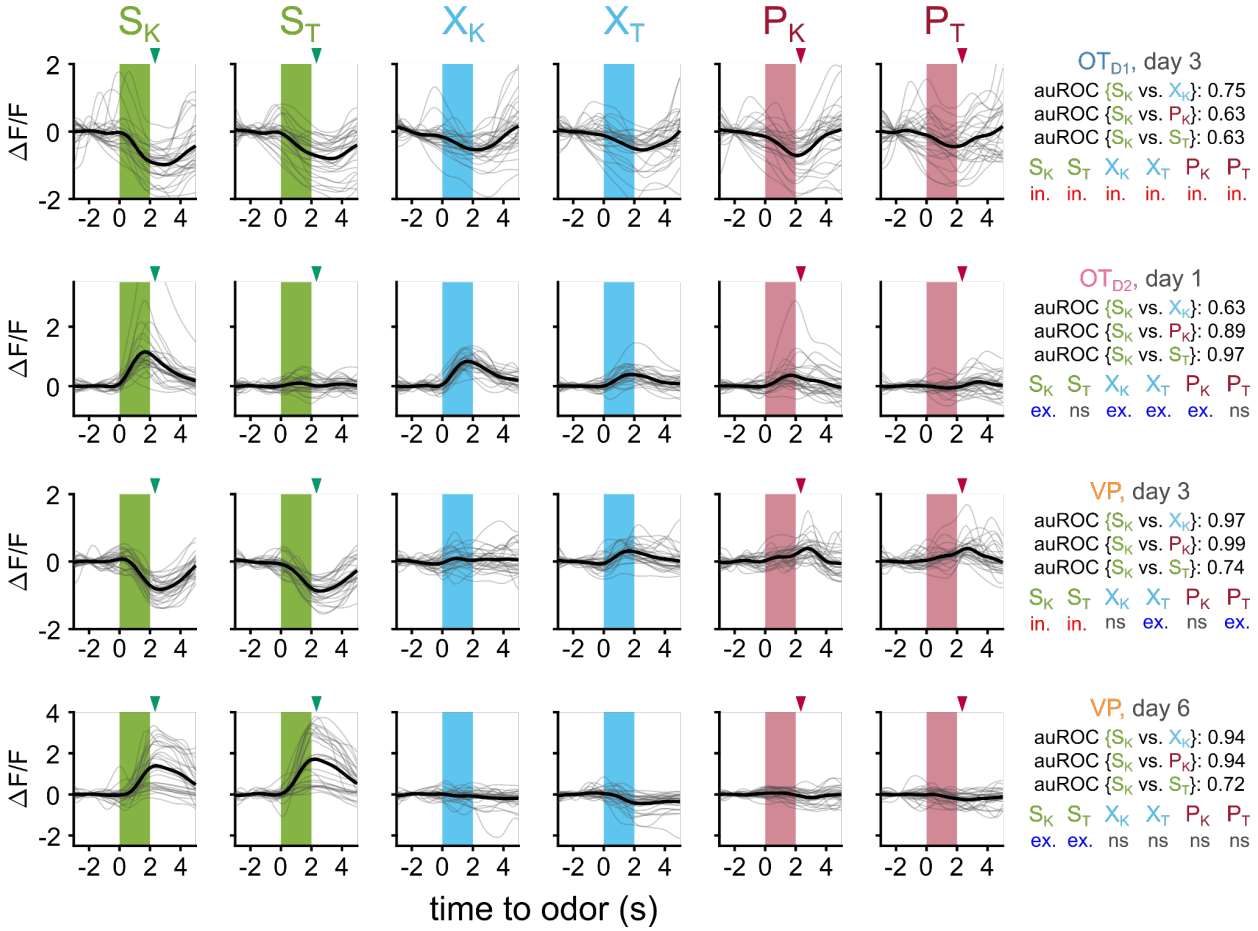
S_K S_T X_K X_T P_K P_T
ΔF/F
time to odor (s)
OT_{D1}, day 3
auROC {S_K vs. X_K}: 0.75
auROC {S_K vs. P_K}: 0.63
auROC {S_K vs. S_T}: 0.63
S_K S_T X_K X_T P_K P_T
in. in. in. in. in. in.
OT_{D2}, day 1
auROC {S_K vs. X_K}: 0.63
auROC {S_K vs. P_K}: 0.89
auROC {S_K vs. S_T}: 0.97
S_K S_T X_K X_T P_K P_T
ex. ns ex. ex. ex. ns
VP, day 3
auROC {S_K vs. X_K}: 0.97
auROC {S_K vs. P_K}: 0.99
auROC {S_K vs. S_T}: 0.74
S_K S_T X_K X_T P_K P_T
in. in. ns ex. ns ex.
VP, day 6
auROC {S_K vs. X_K}: 0.94
auROC {S_K vs. P_K}: 0.94
auROC {S_K vs. S_T}: 0.72
S_K S_T X_K X_T P_K P_T
ex. ex. ns ns ns ns

Figure S7. Traces of example neurons and their corresponding metrics. (**A**) Example traces from an OT_{D1} neuron recorded on day 3. Each column shows this neuron's response to a given odor across 30 trials (gray). The average across all trials is shown in black. For green and red arrowheads mark the time at which sucrose and airpuff were delivered, respectively. auROC values from single-neuron binary classifiers for discriminating {S_K vs. X_K}, {S_K vs. P_K}, and {S_K vs. S_T} are displayed on the right. Additionally, the results of statistical analysis to determine if this neuron reliably responded to each odor (in. = significant inhibitory response, exc. = significant excitatory response, ns= no significant difference between baseline and odor period). (**B**) Example traces from an OT_{D2} neuron recorded on day 1. (**C**) Example traces from a VP neuron recorded on day 3. (**D**) Example traces from a VP neuron recorded on day 6.

Figure S8:

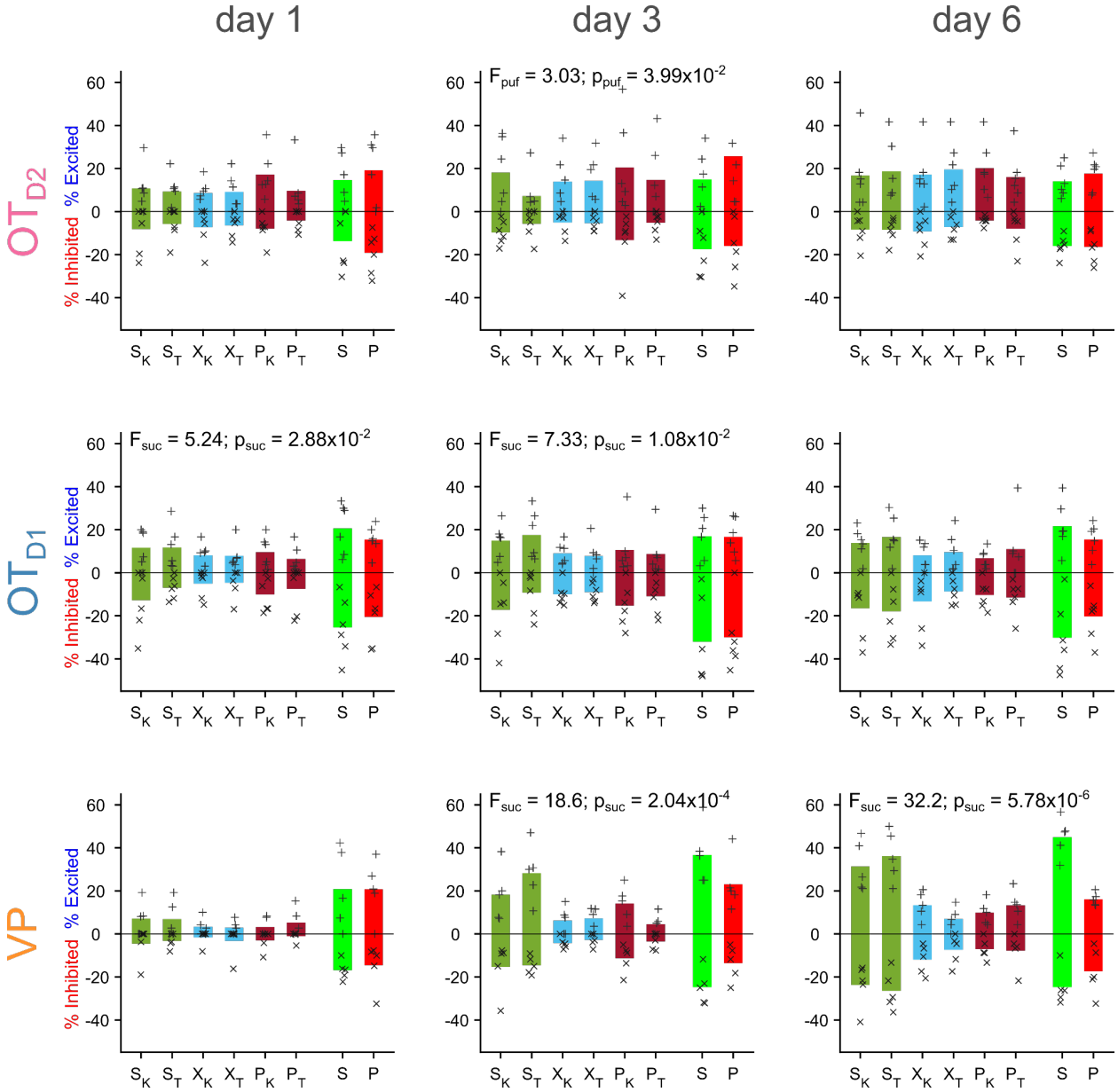
day 1
day 3
day 6
OT D2
OT D1
VP
% Inhibited % Excited
F puf = 3.03; p puf = 3.99x10-2
F suc = 5.24; p suc = 2.88x10-2
F suc = 7.33; p suc = 1.08x10-2
F suc = 18.6; p suc = 2.04x10-4
F suc = 32.2; p suc = 5.78x10-6
S K S T X K X T P K P T S P

Figure S8. Percentage of neurons responsive to each odor across days. Bar graphs showing percentage of neurons from OT_{D2} on day 1 that were significantly excited or inhibited by each odor and each US (S for sucrose, P for airpuff). The average is shown by the bar while the + and x markers show individual biological replicates. For each region and imaging day pair, 3 one-way ANOVA's were run to test for the effect of sucrose, airpuff, or ketone vs. terpene on percentage responsiveness. Only the significant F-statistics are reported with their corresponding p-value.

Figure S9:

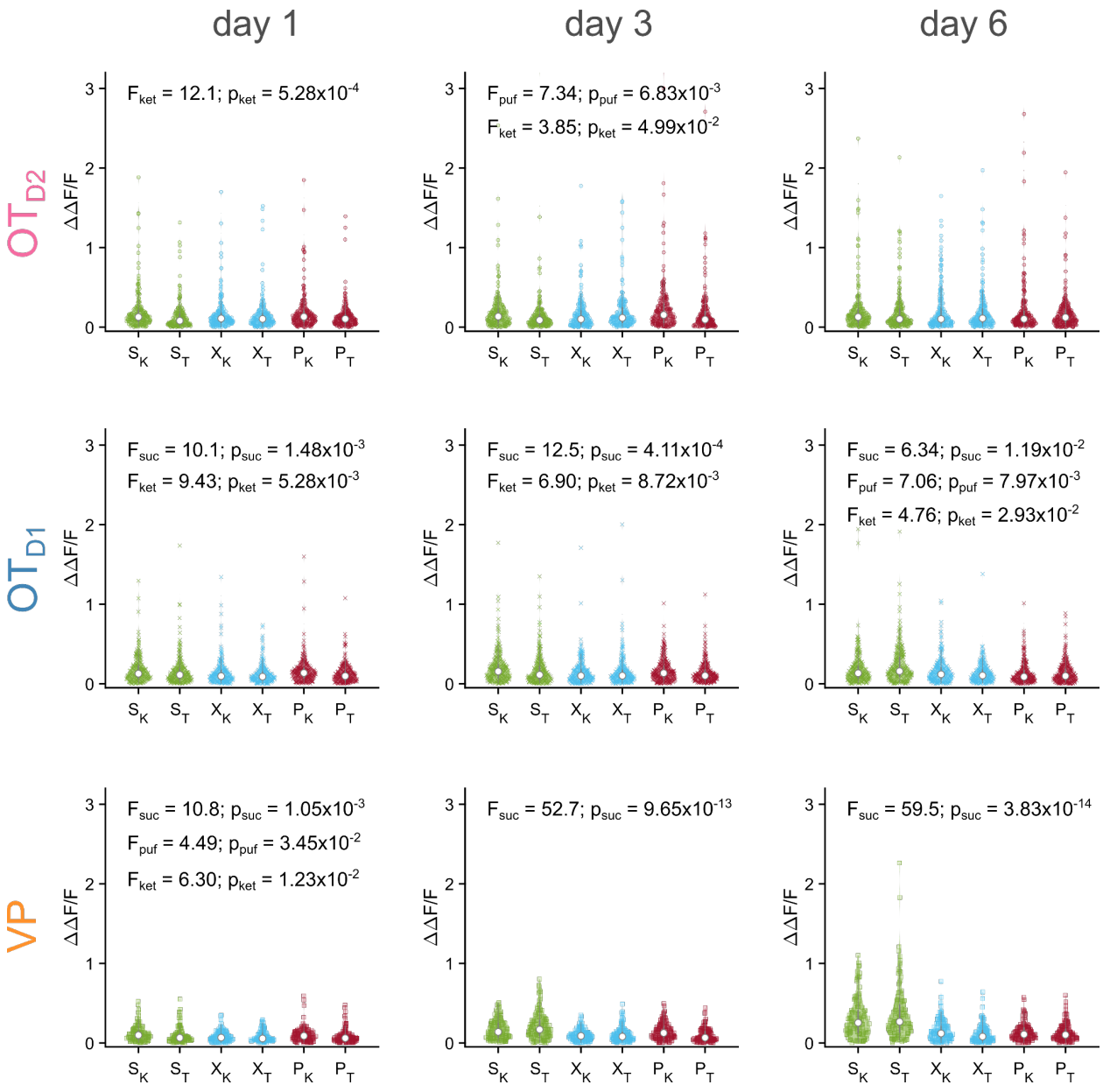
day 1
day 3
day 6
OT D2
OT D1
VP
ΔΔF/F
S K S T X K X T P K P T
F ket = 12.1; p ket = 5.28x10-4
F puf = 7.34; p puf = 6.83x10-3
F ket = 3.85; p ket = 4.99x10-2
F suc = 10.1; p suc = 1.48x10-3
F ket = 9.43; p ket = 5.28x10-3
F suc = 12.5; p suc = 4.11x10-4
F ket = 6.90; p ket = 8.72x10-3
F suc = 6.34; p suc = 1.19x10-2
F puf = 7.06; p puf = 7.97x10-3
F ket = 4.76; p ket = 2.93x10-2
F suc = 10.8; p suc = 1.05x10-3
F puf = 4.49; p puf = 3.45x10-2
F ket = 6.30; p ket = 1.23x10-2
F suc = 52.7; p suc = 9.65x10-13
F suc = 59.5; p suc = 3.83x10-14

Figure S9. Distribution of response magnitudes to each odor across days. Violin plots showing the averaged-over-trials response magnitudes to each odor during the last second of odor exposure. For each region and imaging day pair, 3 one-way ANOVA's were performed to test for the effect of sucrose, airpuff, or ketone vs. terpene on response magnitude. Only the significant F-statistics are reported with their corresponding p-value.

Figure S10:

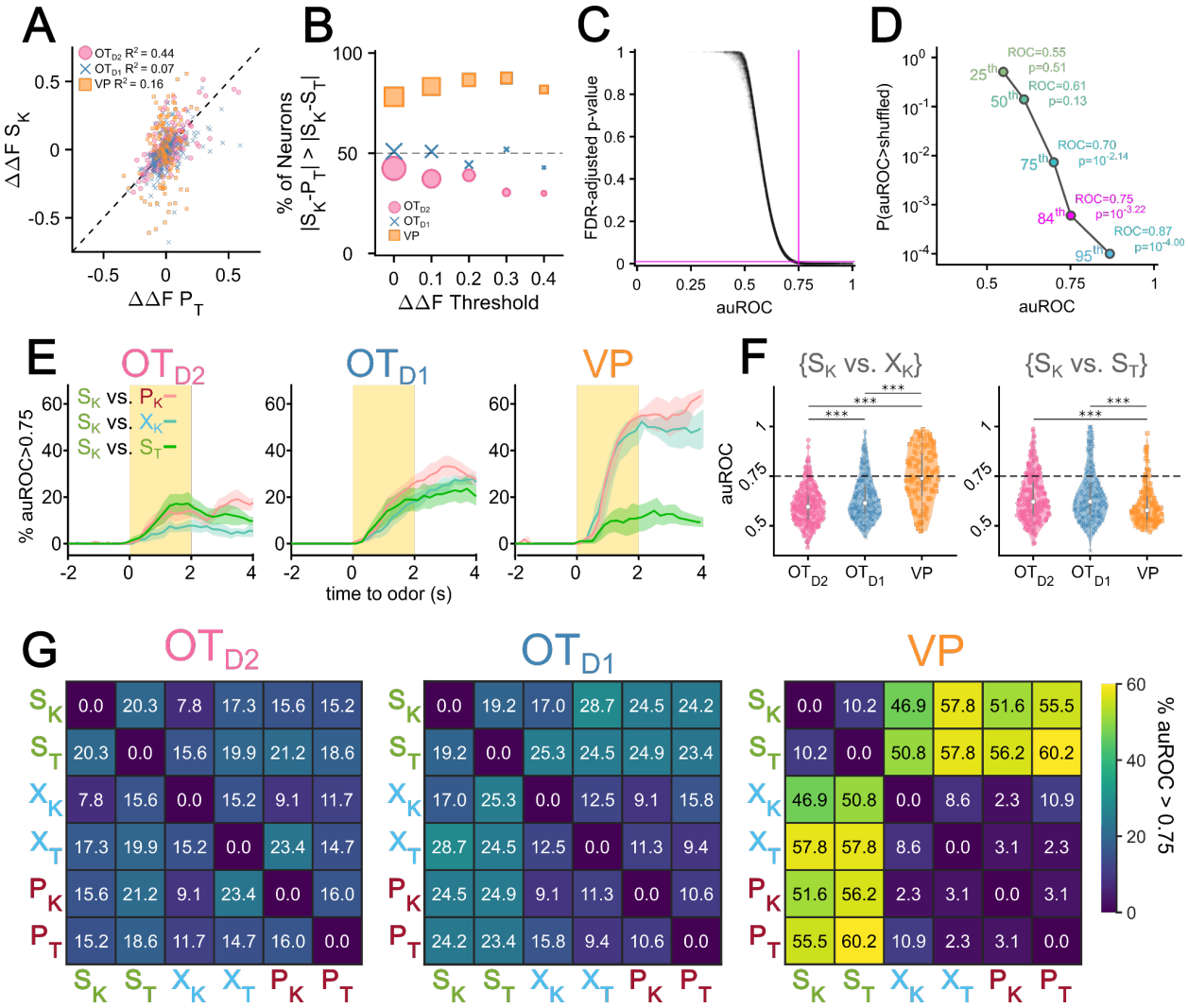
A
OTD2 R² = 0.44
OTD1 R² = 0.07
VP R² = 0.16
ΔΔF SK
ΔΔF PT
B
% of Neurons
|SK-PT| > |SK-ST|
OTD2
OTD1
VP
ΔΔF Threshold
C
FDR-adjusted p-value
auROC
D
P(auROC>shuffled)
ROC=0.55
p=0.51
ROC=0.61
p=0.13
ROC=0.70
p=10^-2.14
ROC=0.75
p=10^-3.22
ROC=0.87
p=10^-4.00
25th
50th
75th
84th
95th
auROC
E
OTD2
OTD1
VP
SK vs. PK
SK vs. XK
SK vs. ST
% auROC>0.75
time to odor (s)
F
{SK vs. XK}
{SK vs. ST}
auROC
***
OTD2
OTD1
VP
G
OTD2
OTD1
VP
SK 0.0 20.3 7.8 17.3 15.6 15.2
ST 20.3 0.0 15.6 19.9 21.2 18.6
XK 7.8 15.6 0.0 15.2 9.1 11.7
XT 17.3 19.9 15.2 0.0 23.4 14.7
PK 15.6 21.2 9.1 23.4 0.0 16.0
PT 15.2 18.6 11.7 14.7 16.0 0.0
SK 0.0 19.2 17.0 28.7 24.5 24.2
ST 19.2 0.0 25.3 24.5 24.9 23.4
XK 17.0 25.3 0.0 12.5 9.1 15.8
XT 28.7 24.5 12.5 0.0 11.3 9.4
PK 24.5 24.9 9.1 11.3 0.0 10.6
PT 24.2 23.4 15.8 9.4 10.6 0.0
SK 0.0 10.2 46.9 57.8 51.6 55.5
ST 10.2 0.0 50.8 57.8 56.2 60.2
XK 46.9 50.8 0.0 8.6 2.3 10.9
XT 57.8 57.8 8.6 0.0 3.1 2.3
PK 51.6 56.2 2.3 3.1 0.0 3.1
PT 55.5 60.2 10.9 2.3 3.1 0.0
SK ST XK XT PK PT
% auROC > 0.75

Figure S10. Pairwise analysis of single neuron odor encoding.

(**A**) Scatterplot comparing the magnitudes of S_K responses ($\Delta\Delta S_K$) to P_T responses ($\Delta\Delta P_T$). The dotted line represents the hypothetical scenario where $\Delta\Delta S_K = \Delta\Delta P_T$. For each population, the R^2 value of the 2-d distribution compared to the $\Delta\Delta S_K = \Delta\Delta P_T$ line is reported. (**B**) The percentage of neurons from each population where the difference between $\Delta\Delta S_K$ and $\Delta\Delta P_T$ is lower than that between $\Delta\Delta S_K$ and $\Delta\Delta S_T$. (**C**) Bootstrapped FDR-adjusted p-values as a function of auROC values of single-neuron binary classifiers. In total, there are 27,900 single-neuron binary classifiers (15 pairwise classifiers for each of the 1860 recordings across 3 regions and days 1, 3 and 6 of imaging). Each classifier was compared against 10,000 shuffles. Horizontal magenta line marks FDR-adjusted p-value of 0.001 and the vertical magenta line marks auROC of 0.75. (**D**) The 25th, 50th, 75th, 84th and 95th percentiles of auROC values and their corresponding unadjusted p-values. For auROC values that were greater than all 10,000 shuffles, a conservative p-value of 0.0001 was assigned. (**E**) The percentage of day 6 {S_K vs P_K}, {S_K vs X_K}, and {S_K vs S_T} auROC values greater than 0.75 as a function of time relative to odor, grouped by region. Lines represent the average across biological replicates and the shaded area shows the SEM. (**F**) Violin plot showing the distribution of pooled day 6 {S_K vs X_K} (left) and {S_K vs S_T} (right) auROC values grouped by region. Horizontal dotted line marks auROC = 0.75. (**G**) Heatmap of percentage of single-neuron pairwise classifiers with auROC>0.75. Classifiers were trained from neural activity recorded during the last second of odor exposure. Percent responsiveness was averaged across animals and grouped by region.

Figure S11:

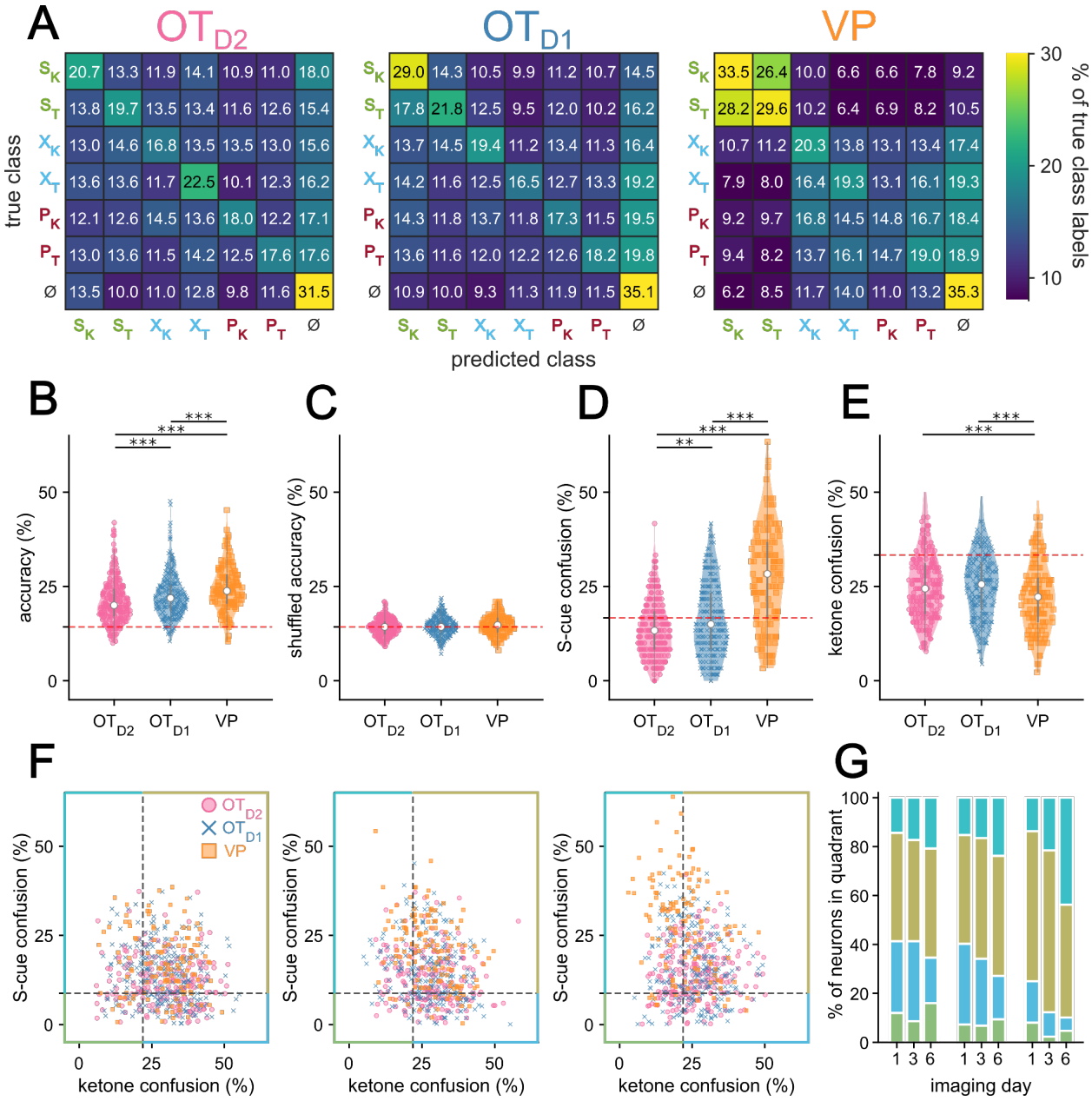
A
OTD2
OTD1
VP
true class
predicted class
% of true class labels
B
C
D
E
accuracy (%)
shuffled accuracy (%)
S-cue confusion (%)
ketone confusion (%)
F
G
% of neurons in quadrant
imaging day

Figure S11. Multinomial analysis of single neuron odor encoding (**A**) Confusion matrix of single-neuron MNR classifiers trained on neural activity during the last second of odor exposure on day 6 of imaging. Rows represent the true class while columns represent the predicted class. Each confusion matrix is averaged across 10 k-fold and across all neurons of a given region. ϕ represents data taken from 30 pre-odor bins randomly sampled from -1.5 to -0.5 seconds relative to odor delivery. (**B**) Violin plot of single-neuron MNR classifier accuracy, averaged across 10 k-fold, grouped by region. (**C**) Violin plot of the single-neuron MNR classifier accuracy trained on shuffled data. Each data point represents the average across 10 shuffles. (**D**) Violin plot of MNR S-cue confusion, i.e. confusion between S_K and S_T. This corresponds to 1) when the true class was S_K but predicted class was S_T and 2) when the true class was S_T but the predicted class was S_K. (**E**) Violin plot of MNR confusion among all ketones. This corresponds when the true class was a ketone and the predicted class was a different ketone (e.g. true class = X_K and predicted class = P_K). (**F**) Scatterplot of each neuron's ketone confusion on the x-axis and S-cue confusion on the y-axis on days 1, 3, and 6 of imaging. (**G**) Stacked bar \graph showing the distribution of neurons from each population that fall into each of the 4 quadrants across the 3 different imaging days.

Figure S12:

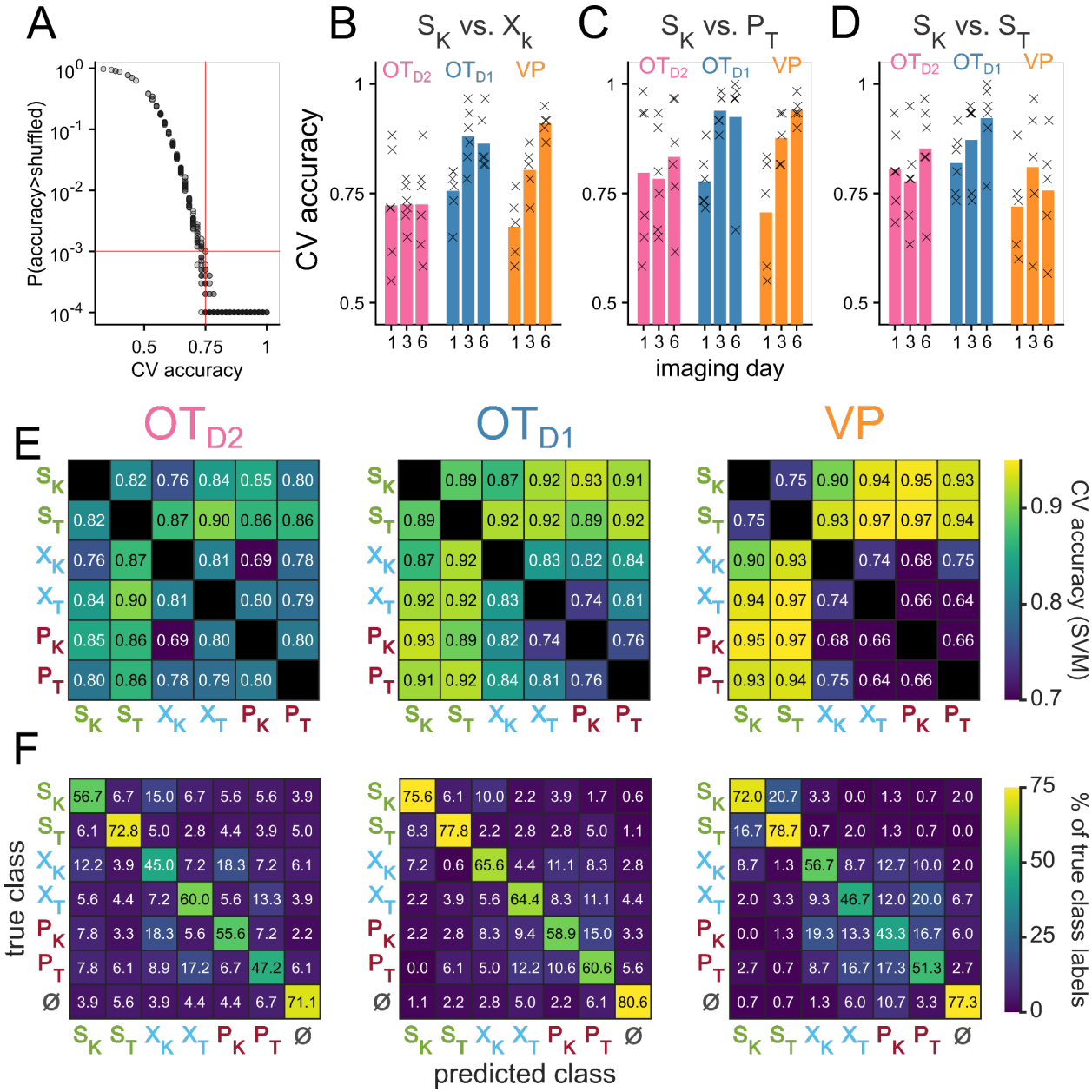
A
P(accuracy>shuffled)
CV accuracy
B
S_K vs. X_k
C
S_K vs. P_T
D
S_K vs. S_T
OT_{D2} OT_{D1} VP
CV accuracy
imaging day
E
OT_{D2}
OT_{D1}
VP
CV accuracy (SVM)
F
true class
predicted class
% of true class labels

Figure S12. Analysis of population-level odor encoding (**A**) Scatterplot of CV-accuracy of linear classifiers trained on simultaneously-recorded neurons on the x-axis and their bootstrapped unadjusted p-values on the y-axis. Red horizontal line marks p = 0.001 and red red vertical line marks CV accuracy = 0.75. All classifiers with CV accuracy higher than 0.75 had p<0.001. In total, there are 765 binary classifiers (15 pairwise classifiers for each of the 51 recordings across 3 regions and days 1, 3, and 6 of imaging). Each classifier was compared against 10,000 shuffles. For auROC values that were greater than all 10,000 shuffles, a conservative p-value of 0.0001 was assigned. (**B**) The CV accuracy for {S_K vs X_K} binary classification trained on the last second of population-level activity. The bars represent the average across biological replicates. CV accuracy from individual animals are shown as x's. (**C**) Same as (B) but for {S_K vs. P_T} classification. (**D**) Same as (B) but for {S_K vs. S_T} classification. (**E**) Heatmap of CV accuracy from binary SVM's trained on day 6 of imaging with a radial basis function kernel. CV accuracy was averaged across biological replicates. (**F**) Confusion matrix of population-level MNR classifiers trained on neural activity during the last second of odor exposure on day 6 of imaging. Rows represent the true class while columns represent the predicted class. Each confusion matrix is averaged across biological replicates. ϕ represents data taken from 30 pre-odor bins randomly sampled from -1.5 to -0.5 seconds relative to odor delivery.

Figure S13:

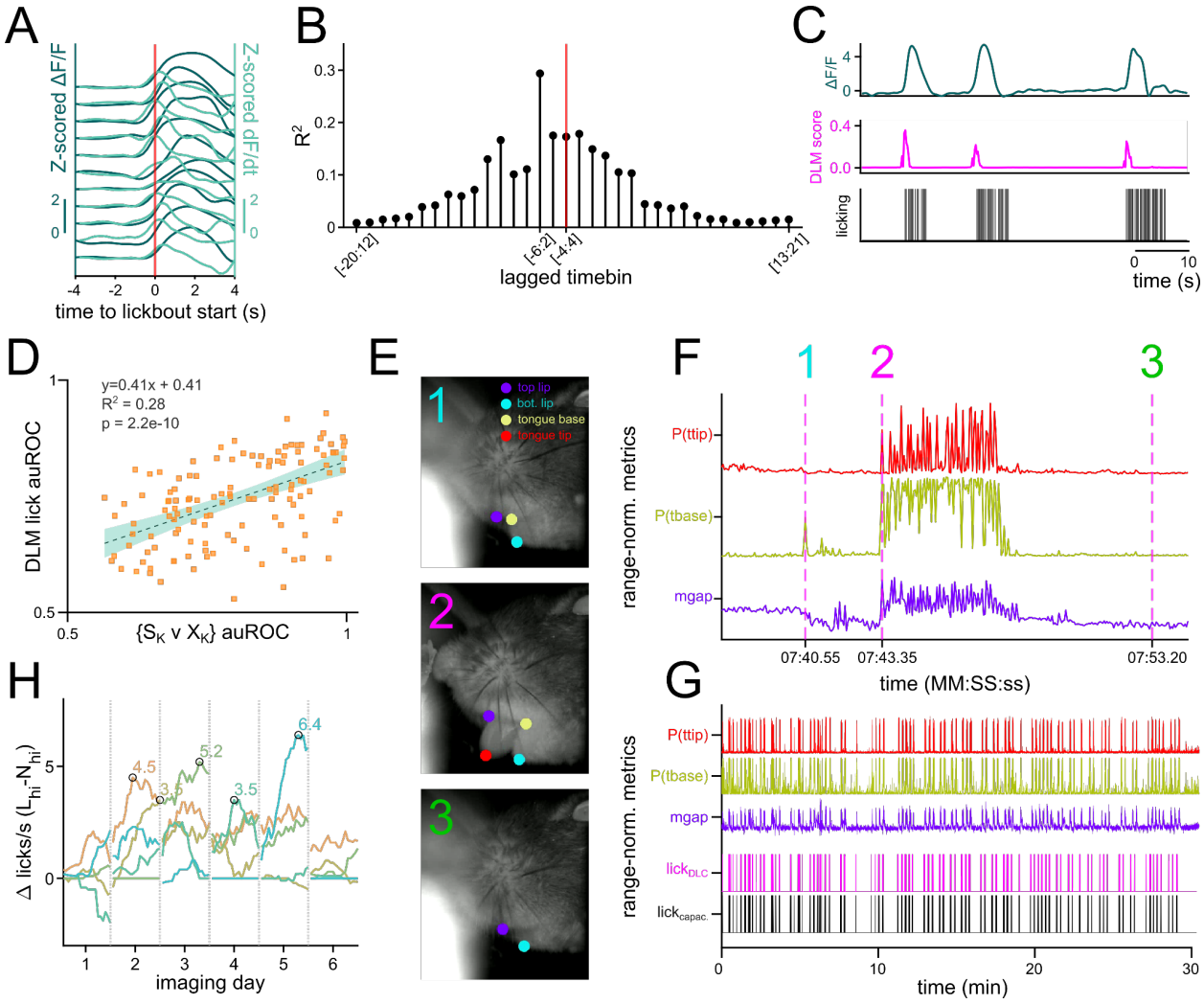
A
Z-scored ΔF/F
Z-scored dF/dt
time to lickbout start (s)
B
R²
lagged timebin
[-20:12]
[-6:2]
[-4:4]
[13:21]
C
ΔF/F
DLM score
licking
time (s)
D
y=0.41x + 0.41
R² = 0.28
p = 2.2e-10
DLM lick auROC
{S_K v X_K} auROC
E
top lip
bot. lip
tongue base
tongue tip
F
range-norm. metrics
P(ttip)
P(tbase)
mgap
07:40.55
07:43.35
07:53.20
time (MM:SS:ss)
G
lick_DLC
lick_capac
time (min)
H
Δ licks/s (L_hi-N_hi)
imaging day

Figure S13. Camera-based detection of licking in head-fixed animals (**A-C**) Metrics of a representative neurons with activity that predicts licking. (**A**) Representative neuron's Z-scored ΔF/F (dark green) and Z-scored dF/dt (light green) aligned to the onset of a lickbout. Each line represents the same neuron's activity during an individual lickbout. (**B**) Stemplot showing an example of the lagged correlation between the onset of licking and the fluorescence of a neuron across 9 frames (1 frame = 0.2s). Time bins of various lags are shown on the x-axis (negative number denotes frames that precede onset of licking) and the resulting R^2 is plotted on the y-axis. Red vertical line marks the case where the 9 frames are centered on the onset of licking. As an example, [-6:2] refers to fluorescence between 1.2 seconds prior to lickbout onset and 0.4 seconds after lickbout onset. (**C**) The output of a distributed lag model (DLM) that predicts the onset of a lickbout from ΔF/F of a single neuron. ΔF/F (dark green, top), DLM score (magenta, middle), and the licking recorded by a capacitive sensor (black, bottom) are shown in parallel. The DLM model was trained using 9 distributed frames ([-6:2]) of ΔF/F for each frame of lickbout onset. (**D**) Scatterplot of day 6 VP neurons' DLM lick classifier auROC on the y-axis plotted against their mean {S_K vs. X_K} auROC on the x-axis. The slope, intercept, R^2, and p-value of the slope are shown on the top left corner. (**E**) 3 example snapshots of the camera feed during moving lick spout paradigm with overlay of DeepLabCut labeling. The coordinates of top lip, bottom lip, base of tongue (tbase), and tip of tongue (ttip) are displayed with a probability cutoff of 0.4. (**F**) Range-normalized metrics from DLC labeling. P(ttip) (red, top) is the probability score assigned to the labeling of the tongue tip. P(tbase) (yellow, middle) is the probability score assigned to the labeling of the tongue base. Mgap (purple, bottom) is the Euclidean distance between the top lip and the bottom lip. The 3 vertical magenta lines represent the timing of the 3 snapshots shown in (E). (**G**) The same range-normalized metrics as in (F) plotted against the ground truth licking data from capacitive sensor (black, bottom) and DLC-based licking classifier score (magenta, second from bottom). (**H**) Lineplot showing the difference in total licking to L_{hi} nd N_{hi} during the time bin (1.5-2.5 seconds after odor onset) used for most analyses plotted against imaging day for individual animals. The time of peak difference is circled in black.